



RADIOACTIVITY AND THERMALIZATION IN THE EJECTA OF COMPACT OBJECT MERGERS AND THEIR IMPACT ON KILONOVA LIGHT CURVES

JENNIFER BARNES¹, DANIEL KASEN^{1,2}, MENG-RU WU³, AND GABRIEL MARTÍNEZ-PINEDO^{3,4}

¹ Departments of Physics and Astronomy, 366 LeConte Hall, University of California, Berkeley, CA 94720, USA; jlbarne@berkeley.edu

² Nuclear Science Division, Lawrence Berkeley National Laboratory, Berkeley, CA 94720, USA

³ Institut für Kernphysik (Theoriezentrum), Technische Universität Darmstadt, Schlossgartenstraße 2, D-64289 Darmstadt, Germany

⁴ GSI Helmholtzzentrum für Schwerionenforschung, Planckstraße 1, D-64291 Darmstadt, Germany

Received 2016 May 23; revised 2016 July 25; accepted 2016 July 25; published 2016 September 28

ABSTRACT

One promising electromagnetic signature of compact object mergers are kilonovae: approximately isotropic radioactively powered transients that peak days to weeks post-merger. Key uncertainties in kilonova modeling include the emission profiles of the radioactive decay products—non-thermal β -particles, α -particles, fission fragments, and γ -rays—and the efficiency with which their kinetic energy is absorbed by the ejecta. The radioactive energy emitted, along with its thermalization efficiency, sets the luminosity budget and is therefore crucial for predicting kilonova light curves. We outline uncertainties in the radioactivity, describe the processes by which the decay products transfer energy to the ejecta, and calculate time-dependent thermalization efficiencies for each particle type. We determine the net thermalization efficiency and explore its dependence on r -process yields—in particular, the production of α -decaying translead nuclei—and on ejecta mass, velocity, and magnetic fields. We incorporate our results into detailed radiation transport simulations, and calculate updated kilonova light curve predictions. Thermalization effects reduce kilonova luminosities by a factor of roughly 2 at peak, and by an order of magnitude at later times (15 days or more after explosion). We present analytic fits to time-dependent thermalization efficiencies, which can be used to improve light curve models. We revisit the putative kilonova that accompanied gamma-ray burst 130603B, and estimate the mass ejected in that event. We find later time kilonova light curves can be significantly impacted by α -decay from translead isotopes; data at these times may therefore be diagnostic of ejecta abundances.

Key words: nuclear reactions, nucleosynthesis, abundances – radiative transfer – stars: black holes – stars: neutron

1. INTRODUCTION

In addition to producing kilohertz gravitational waves (GW) detectable by ground-based interferometers (Abadie et al. 2010), compact object (CO) mergers involving a neutron star (NS) are likely to emit a variety of electromagnetic (EM) signals. Immediately post-merger, the accretion of disrupted NS material onto the central black hole (BH) or hypermassive NS may drive a short gamma-ray burst (Paczynski 1986; Eichler et al. 1989; Narayan et al. 1992). Mergers may also produce optical/infrared transients (Li & Paczyński 1998; Metzger et al. 2010; Roberts et al. 2011; Barnes & Kasen 2013) powered by the radioactive decay of heavy elements synthesized via rapid neutron capture (the r -process; Arnould et al. 2007). The r -process is expected to operate in material ejected from the system dynamically (Lattimer & Schramm 1974, 1976; Freiburghaus et al. 1999; Rosswog et al. 1999; Goriely et al. 2011; Korobkin et al. 2012), or unbound from a remnant accretion disk (Fernández & Metzger 2013; Perego et al. 2014; Just et al. 2015). On much longer timescales, the interaction of the ejecta with the interstellar medium will generate a radio signal (Nakar & Piran 2011).

Observing an EM counterpart will enhance the science returns of a GW detection (Metzger & Berger 2012) by identifying the host galaxy and the position of the merger within the host (Holz & Hughes 2005; Dalal et al. 2006; Nissanke et al. 2013; Kasliwal & Nissanke 2014), constraining the NS equation of state (Bauswein et al. 2013, 2015; Hotokezaka et al. 2013), and confirming low signal-to-noise GW events (Kochanek & Piran 1993; Harry & Fairhurst 2011). Among possible counterparts, the radioactive transients—

known as “kilonovae”—are especially promising. Kilonova emission is roughly isotropic (Roberts et al. 2011; Bauswein et al. 2013), and peaks on timescales of days to weeks post-merger (Barnes & Kasen 2013; Tanaka & Hotokezaka 2013; Grossman et al. 2014), making it ideal for EM follow-up of a GW trigger. Because kilonovae derive their energy from radioactive decay, they probe nucleosynthesis in the merger in a way other counterparts cannot, and may therefore constrain the astrophysical origin of r -process element production.

Accurate models of kilonova photometry are crucial for dual detection efforts. Unfortunately, the exotic composition of the heavy element ejecta, and uncertainties in r -process nucleosynthesis and decay, pose challenges to radiation transport simulations required to build these models. Recent work (Kasen et al. 2013) clarified the opacity of r -process material, reducing a major uncertainty in kilonova radiation transport simulations, but other key inputs remain relatively unconstrained.

Any rigorous kilonova model must address the following aspects of radioactivity: (i) the total amount of radioactive energy released; (ii) the decay channels that dominate the energy production during different phases of kilonova evolution; and (iii) the efficiency with which suprathermal radioactive decay products— β -particles, α -particles, γ -rays, and fission fragments—transfer their energy to the thermal background. Once thermalized, the energy is re-radiated as thermal emission, powering the kilonova light curve.

Although thermalization determines the kilonova’s luminosity, and is thus essential for light curve modeling, no detailed calculation of thermalization efficiencies has been attempted.

Metzger et al. (2010) presented analytic estimates of thermalization, but focused on timescales shorter than those now believed to characterize kilonova light curves. Hotokezaka et al. (2016) studied γ -ray deposition in kilonovae, but did not investigate the thermalization of charged particles, which carry a large fraction of the radioactive energy.

Modeling the thermalization of r -process decay energy in the kilonova ejecta is challenging. Thermalization rates are sensitive to the ejecta's mass, velocity, and composition, as well as its magnetic field structure, which has not been definitively determined by magnetohydrodynamic simulations. The broad range of elements synthesized by the r -process, and the often unknown properties of the heaviest of those elements, complicates the situation, as does the complexity of the net emission spectrum, which is a sum over several decay chains, each evolving on its own timescale.

This paper addresses the issues outlined above, with special emphasis on the key physical processes influencing the thermalization of r -process decay products in kilonovae. In Section 2, we describe our ejecta model and its uncertainties. Section 3 defines energy-loss rates for β -particles, α -particles, γ -rays, and fission fragments, and explores their sensitivity to ejecta parameters. Analytic estimates and analytic expressions for thermalization efficiencies are developed in Section 4. In Section 5, we present detailed numerical calculations of time-dependent thermalization efficiencies $f(t)$ for individual species and for the system as a whole, and discuss the sensitivity of $f(t)$ to properties of the ejecta. Finally, Section 6 evaluates the effect of thermalization on kilonova light curves, and uses improved light curve models to estimate the mass ejected by the claimed kilonova associated with GRB 130603B.

2. PROPERTIES OF THE KILONOVA EJECTA

2.1. Ejecta Model

Predictions of kilonova outflows vary, due to natural diversity in the merging systems (e.g., different mass ratios, BHNS versus NS²) and uncertainties in the NS EOS. Recent hydrodynamic simulations (Bauswein et al. 2013; Hotokezaka et al. 2013; Kyutoku et al. 2015; Sekiguchi et al. 2016) suggest that mergers dynamically eject between $\sim 10^{-4}$ and a few $\times 10^{-2} M_{\odot}$ of material, with bulk velocities of a few tenths the speed of light. Additional material ($\sim 10^{-3}$ – $10^{-2} M_{\odot}$) can exit the system at slightly lower velocities (0.05 c –0.1 c) as a wind from an accretion torus (Fernández & Metzger 2013; Perego et al. 2014; Fernández et al. 2015; Just et al. 2015).

We adopt as our fiducial model a system with $M_{\text{ej}} = 5 \times 10^{-3} M_{\odot}$ and $v_{\text{ej}} = 0.2c$, where v_{ej} is defined in terms of the explosion kinetic energy, $E_k = M_{\text{ej}} v_{\text{ej}}^2 / 2$. Since denser ejecta configurations thermalize more efficiently than diffuse systems, we vary these parameters over the ranges $M_{\text{ej}}/M_{\odot} \in [10^{-3}, 5 \times 10^{-2}]$ and $v_{\text{ej}}/c \in [0.1, 0.3]$.

We assume the ejecta is spherical and expanding homologously, and that the density profile follows a broken power law, declining with velocity coordinate $v = r/t$ as $v^{-\delta}$ in the inner regions of the ejecta, and v^{-n} , $n > \delta$, in the outer regions. We set $\delta = 1$ and $n = 10$. Barnes & Kasen (2013) provides a complete mathematical description of the density profile.

2.2. Magnetic Fields

Kilonova ejecta contain a residual magnetic field, either inherited directly from the parent NSs, or seeded by amplified fields produced by turbulence during the merger or in the resultant accretion disk (Kiuchi et al. 2014, 2015). Though weakened by expansion, the fields remain strong enough to influence charged particle motion. In a sufficiently strong field, charged particles have Larmor radii smaller than the coherence length of the magnetic field, and their motion is confined to “flux tubes” that trace the field lines.

If magnetic flux is frozen into the homologously expanding ejecta, the field strength is related to the ejecta radius $R_{\text{ej}} = v_{\text{ej}} t$ by

$$B(t) \approx \frac{B_0 R_0^2}{R_{\text{ej}}^2} \approx 3.7 \times 10^{-6} B_{12} R_6^2 v_2^{-2} t_d^{-2} \text{ G}, \quad (1)$$

where $v_2 = v/0.2c$, t_d is the elapsed time in days, and B_0 and R_0 are the magnetic field and radius at the time of mass ejection. The quantities $B_{12} = B_0/10^{12} \text{ G}$ and $R_6 = R_0/10^6 \text{ cm}$ have been scaled to typical values; $R_0 \approx 10^6$ to 10^7 cm is characteristic of the size of NSs or the post-merger accretion disk, and B_0 may range from 10^9 to 10^{15} G , depending on the initial NS fields and the efficiency of magnetic field amplification.

A relativistic particle of mass m , charge q , kinetic energy E , and velocity v in a magnetic field B has a maximum Larmor radius (when $v \perp B$) of

$$r_{\text{L,max}} = \frac{(E + mc^2)v}{qBc}.$$

Assuming typical emission energies of $E_{\beta,0} = 0.5 \text{ MeV}$ for β -particles, $E_{\alpha,0} = 10 \text{ MeV}$ for α -particles, and $E_{\text{ff},0} = 150 \text{ MeV}$ for fission fragments, and assuming fission fragments are singly ionized and have masses of $\sim 130 m_u$, with m_u the atomic mass unit, the Larmor radii are

$$\frac{r_{\text{L,max}}(t)}{R_{\text{ej}}(t)} = \begin{cases} 1.5 \times 10^{-6} v_2 t_d B_{12}^{-1} R_6^{-2} & \beta\text{-particles} \\ 2.4 \times 10^{-4} v_2 t_d B_{12}^{-1} R_6^{-2} & \alpha\text{-particles} \\ 1.0 \times 10^{-2} v_2 t_d B_{12}^{-1} R_6^{-2} & \text{fiss. fragments.} \end{cases} \quad (2)$$

We will adopt the flux tube approximation for all particles. This is clearly appropriate for α - and β -particles, which have $r_{\text{L}}/R_{\text{ej}} \ll 1$ for the duration of the kilonova. Fission fragments may, at later times, have r_{L} large enough that they jump from field line to field line. We discuss this possibility in Appendix A.3.2, but do not employ models of fission fragment transport beyond the flux tube approximation in this work.

The magnetic field structure determines charged particle trajectories and so affects thermalization. Radial fields can escort fast charged particles straight out of the ejecta, reducing thermalization. In contrast, toroidal or tangled fields trap charged particles, and so enhance thermalization. We consider three types of configurations here: radial ($\mathbf{B} \propto \hat{\mathbf{r}}$), which may be produced by the outward motion of the ejecta “combing” out the field lines; toroidal ($\mathbf{B} \propto \hat{\phi}$), perhaps created by the spiral motion of NSs shedding mass through tidal stripping; and random, which may be generated by turbulent motions in the material during mass ejection. To model the latter case, we assume field lines randomly re-orient on a length scale λR_{ej} , where the dimensionless parameter $\lambda < 1$.

2.3. Composition

The ejecta composition impacts thermalization in two ways. First, it determines the partition of radioactive energy among different decay channels, and the energy spectra of the decay products. Second, it sets the properties of the background material (e.g., isotope mass, atomic number, and ionization energy) which influence the energy-loss rates of the decay products.

To determine the ejecta composition, we calculate r -process nucleosynthesis on a set of smoothed-particle hydrodynamics (SPH) trajectories extracted from a relativistic simulation of an equal-mass ($1.35 M_{\odot}$ – $1.35 M_{\odot}$) NS² merger (Goriely et al. 2011). At the start of the nucleosynthesis calculation, all trajectories had temperatures of 6 GK, densities set by their hydrodynamical histories, compositions determined by nuclear statistical equilibrium, and initial electron fractions $Y_{e,0}$ between 1.5×10^{-2} and 5.5×10^{-2} . These quantities were then evolved according to the reaction network, which tracks charged particle reactions, neutron capture, photodissociation, β - and α -decay, and fission, for more than 7300 nuclei. (For a detailed description of the network, see Mendoza-Temis et al. 2015).

The hydrodynamical model predicts two classes of trajectories that produce two distinct compositions: “slow” trajectories, where all free neutrons are depleted by neutron-capture, and “fast” trajectories, where early rapid expansion precludes the capture of all neutrons by seed nuclei (see also Goriely et al. 2014; Just et al. 2015; Mendoza-Temis et al. 2015; Metzger et al. 2015). The slow trajectories comprise $\sim 90\%$ of the ejecta, and robustly produce r -process elements up to the third peak. The fast ejecta r -pattern is different from the slow component due to the longer neutron-capture timescale. In constructing our ejecta model, we assume that at times relevant for thermalization, material from slow trajectories will be located in the ejecta’s interior regions (henceforth “inner ejecta”), while material from the fast trajectories occupies the outer regions (“outer ejecta”). We sum the trajectories in each class to construct mass-integrated inner and outer compositions. We also select a representative case from the set of inner trajectories, which typifies conditions in the merger ejecta. We use this representative trajectory to study the details of the radioactivity.

The top panel of Figure 1 shows the inner ejecta composition at $t = 1$ day, based on neutron-capture and photodissociation rates computed using the statistical model for four different nuclear mass models: the Finite Range Droplet Model (FRDM; Möller et al. 1995), the Hartree–Fock–Bogoliubov model HFB21 (Goriely et al. 2010), the Weizsäcker–Skyrme model (WS3; Liu et al. 2011), and the Duflo–Zucker model with 31 parameters (DZ31; Duflo & Zuker 1995). We find that although the abundance pattern is similar for different mass models, particularly around $A \sim 130$ due to fission cycling, the position of the peak at $A \sim 195$ and the abundances for $A \gtrsim 195$ depend on the mass model. The differences in the translead abundances impact the late-time kilonova light curves, as will be discussed in Section 6.4.

The abundances are also influenced by the electron fraction $Y_{e,0}$ at the onset of the r -process; neutron scarcity (high $Y_{e,0}$) suppresses the assembly of the heaviest r -process elements. Our SPH trajectories are all initially very neutron-rich; however, weak interactions in the aftermath of a merger could raise $Y_{e,0}$ substantially (Wanajo et al. 2014; Goriely et al. 2015;

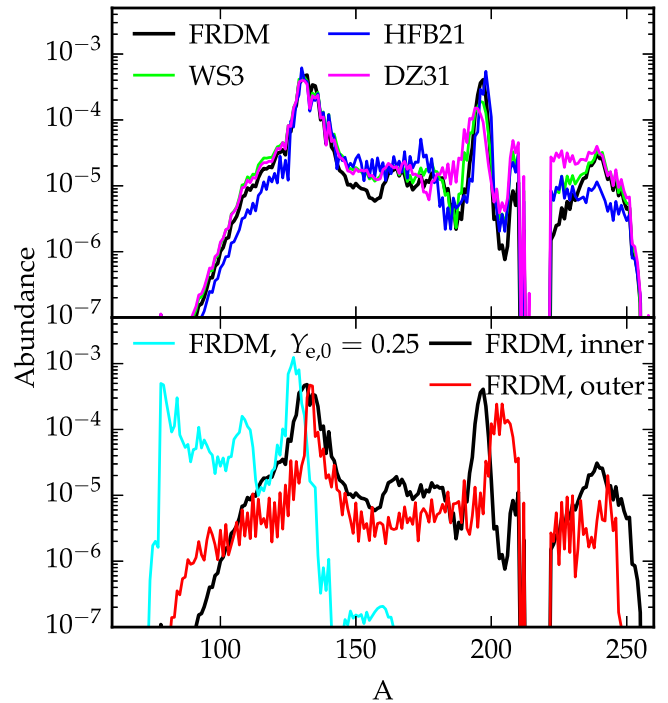


Figure 1. Abundance yields from our nuclear network calculations at $t = 1$ day. Top panel: mass-integrated abundances from the “inner” ejecta ($\sim 90\%$ of the ejected mass) for four nuclear mass models. The r -process proceeds past the third peak, and strong fission cycling reduces differences among nuclear mass models. Bottom panel: an illustration of major factors affecting the final abundances. The red curve shows mass-integrated abundances for the “outer” ejecta, using the FRDM mass model. Rapid expansion hinders free neutron capture, decreasing heavy element production, and creating a substantial amount of hydrogen as uncaptured neutrons decay to protons. The cyan curve shows the abundance yield of a representative inner ejecta trajectory, whose initial electron fraction has been artificially increased to $Y_{e,0} = 0.25$, leading to limited production of nuclei with $A > 130$.

Sekiguchi et al. 2015). To explore this effect, we artificially increased the initial $Y_{e,0}$ of our representative trajectory from its value of 0.04, and reran the nuclear reaction network. As expected, higher initial electron fractions produce fewer heavy elements (bottom panel of Figure 1) and for $Y_{e,0} \gtrsim 0.2$ the r -process fails to reach the third peak, instead producing material with $A \sim 70$ – 110 .

The ejecta composition evolves with time as neutron-rich isotopes gradually decay to stability. However, on timescales relevant for kilonova light curves ($t \sim 0.1$ – 10 days), this evolution is fairly slow, and driven primarily by α - and β -decays, which do not dramatically change the abundance-averaged properties of the composition. For the purpose of calculating energy-loss rates, we therefore assume that the abundance-averaged properties are constant in time, but vary in space, with the inner 90% (outer 10%) of the mass described by the average abundance pattern of the inner (outer) trajectories, calculated at $t = 1$ day using the FRDM mass model. The outer ejecta differs from the inner ejecta primarily in its high abundance of hydrogen, produced by the decay of remnant free neutrons to protons.

2.4. Radioactivity

The energy-generation rate from r -process decay has been shown to approximately follow $\dot{\epsilon} = \epsilon_0 t_d^{-\eta}$, with

$\epsilon_0 \approx 10^{11}$ ergs $s^{-1}g^{-1}$ and $\eta = 1.1\text{--}1.4$ (Metzger et al. 2010; Goriely et al. 2011; Roberts et al. 2011; Korobkin et al. 2012). However, the fraction of the energy supplied by each decay channel and the emission spectra for each decay product are less clear.

Though r -process radioactivity is most commonly associated with β -decay, any translead nuclei synthesized will decay by α -emission, and heavier ($A \gtrsim 250$) nuclei may undergo fission, trends which have implications for thermalization. Radioactive emission in kilonovae will at all times be dominated by isotopes with half-lives $\tau_{1/2}$ of the order of t_{\exp} , the time since explosion. For any particular decay channel, $\tau_{1/2}$ is strongly correlated with the energy Q emitted when a nucleus decays. However, this is not true across decay channels; for a given $\tau_{1/2}$, β -decay has a lower Q than α -decay, which has a lower Q than fission. As a result, α -decay can generate a substantial fraction of the r -process radioactive energy, even though r -process yields are dominated by nuclei that β -decay. Fission could, in principle, also be an important source of energy, but we find almost all fissioning nuclei have $\tau_{1/2}$ less than a day, suggesting that fission supplies a negligible amount of energy after very early times. Since energy from α -decay thermalizes with a different efficiency than β -decay energy, thermalization depends on the relative importance of these decay channels, and thus on the yields of translead nuclei.

The top panel of Figure 2 shows the fraction of radioactive energy produced by α -decay, β -decay, and fission, for the representative trajectory introduced in Section 2.3, calculated for four nuclear mass models. β -decay is the primary source of energy for all mass models out to late times. Fission, including β -delayed, neutron-induced, and spontaneous fission, contributes $\sim 10\%$ of the energy at times $\lesssim 1$ day, and α -decay becomes significant within a few hours. The fractions for the different nuclear mass models generally agree with each other, but the estimates of energy generated by α -decay differ by a factor of almost 10, with DZ31 predicting the largest contribution from α -decay and FRDM predicting the least. Since α -decays release more energy, per decay, than β -decay, the enhanced role of α -decay predicted by the DZ31 model also results in an increase in the total energy generated by the decay of r -process isotopes. The increase is modest early on (a factor of $\lesssim 1.2$ for $t \lesssim 1$ day), but becomes more important at late times (a factor of $\gtrsim 2$ by $t = 1$ month.)

The bottom panel of Figure 2 explores the effect of electron fraction on the decay channels. Fission and α -decay are significant sources of energy for $t \lesssim 1$ day and $t \gtrsim 1$ day, respectively, for ejecta with $Y_{e,0} \lesssim 0.2$, but become negligible at higher $Y_{e,0}$ because the reduced number of free neutrons chokes the production of the heaviest nuclei.

2.5. Emission Spectra of Decay Products

Modeling the energy spectra of r -process radioactive decay products is complicated by the large number of decay chains and the uncertain nuclear data. However, we can construct approximate spectra by considering emission from a range of contributing decays. We calculate emission spectra using the time-dependent composition of our representative inner SPH trajectory. The decay energies for α - and β -decay were determined from experimental mass excesses (AME 2012; Audi et al. 2012; Wang et al. 2012) when available, and theoretical (FRDM) mass excesses otherwise. Decay data, including β endpoint energies, γ -spectra, and half-lives for β -

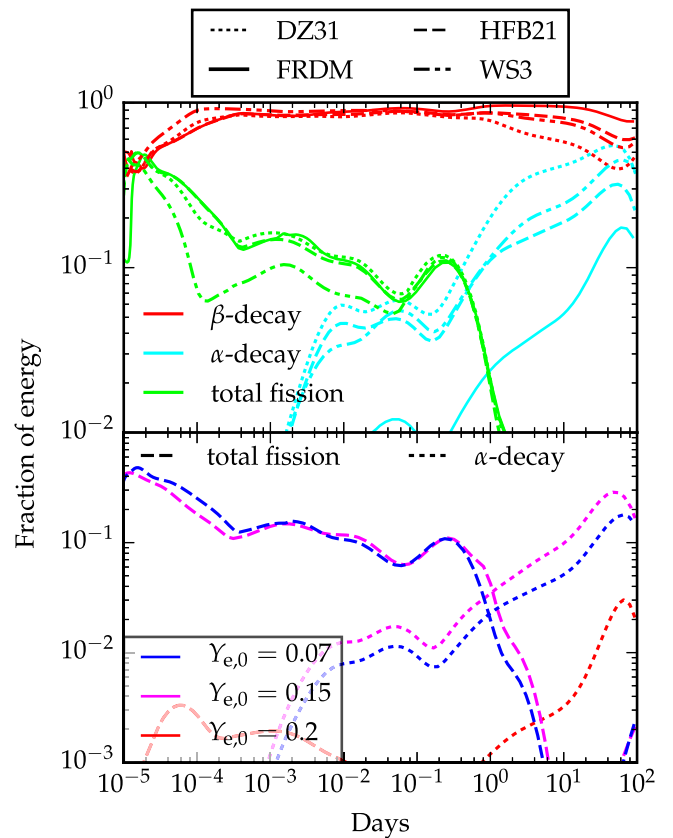


Figure 2. Top panel: the fraction of the total radioactive energy produced by β -decays, α -decays, and fission in our representative trajectory for four nuclear mass models. While β -decay dominates, fission (α -decay) can be important at early (late) times. Agreement between the four mass models studied is within an order of magnitude. Bottom panel: energy released in α -decays and fission, for the FRDM mass model, for a range of $Y_{e,0}$. Lower electron fractions favor the assembly of the heavy elements that later decay by fission and α -emission. As $Y_{e,0}$ increases, these processes become less important, and are negligible for $Y_{e,0} > 0.2$.

and α -decay, were retrieved from the Nuclear Science References database (Pritychenko et al. 2011), accessed via the website of the International Atomic Energy Agency.

2.5.1. Beta Decay

Energy from β -decay takes the form of energetic β -particles, γ -rays, and neutrinos. (β -delayed fission is treated as part of fission, and we neglect β -delayed neutron and α -emission, as they are expected to be negligible for nuclei with lifetimes longer than a day.) Following β -emission, nuclear de-excitation can also emit low-energy atomic electrons, delayed neutrons, and \sim keV X-rays, but we found that these secondary processes were negligible.

We constructed β - and γ -spectra using selected isotopes that dominated the β -decay energy production. The energy-generation rate of an isotope i was estimated as $\dot{\epsilon}_{\beta,i} = Y_i Q_{\beta,i}/\tau_{1/2,i}$, where Y_i is the number abundance of the isotope, $Q_{\beta,i}$ the decay energy, and $\tau_{1/2,i}$ the half-life. We used experimental values for Q_β and $\tau_{1/2}$ when available, and theoretical values otherwise. We excluded isotopes lacking decay data and those with heating rates less than 1% of the maximum single-isotope heating rate. The excluded β -decays account for only 5%–7% of the total β -decay energy at all times. The γ -ray intensities were taken directly from nuclear

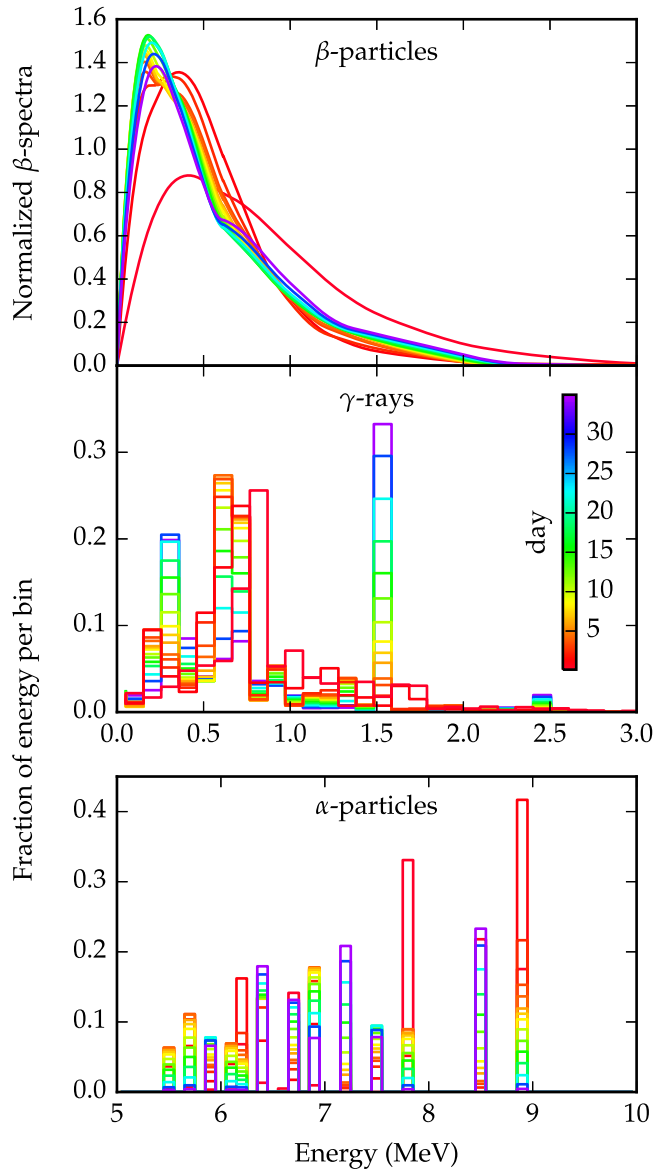


Figure 3. Emission spectra for β -particles (top panel), γ -rays (middle panel), and α -particles (bottom panel) as a function of time.

measurements, while β -spectra were constructed from endpoint energies and intensities assuming all decays had an allowed spectral shape and using the simplified Fermi formula fit proposed by Schenter & Vogel (1983).

We find that roughly 20% of the β -decay energy emerges as β -particles, 45% as γ -rays and 35% as neutrinos. The energy lost to neutrinos, which escape the ejecta without depositing any energy, sets an upper limit of $\sim 65\%$ on the β -decay thermalization efficiency. The top two panels of Figure 3 show the β - and γ -spectra for the composition of our neutron-rich representative SPH trajectory for $t = 1$ –30 days. The γ -ray spectra peak at several hundred keV and the β -spectra at around 0.5 MeV.

The β -spectrum was found to be consistent across mass models, which is not surprising since β -decay energy is very sensitive to half-life, and β -emission at all times is dominated by nuclei with half-lives roughly equal to the time since explosion. However, we did find that the spectrum depends

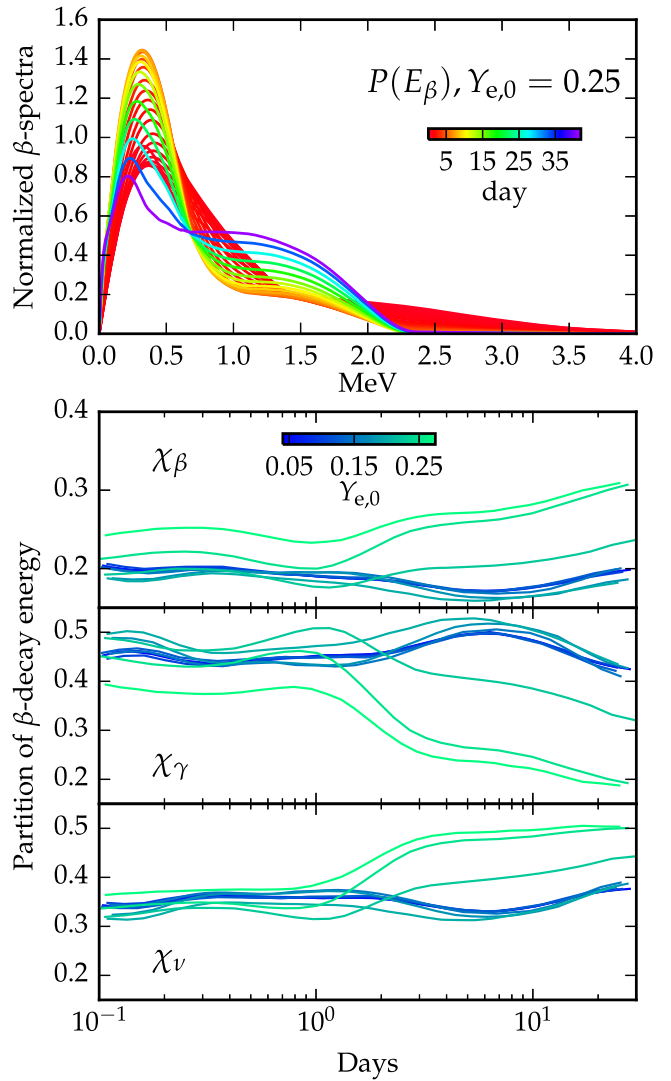


Figure 4. Effect of electron fraction $Y_{e,0}$ on β -decay for the FRDM nuclear mass model. (Other nuclear mass models studied showed similar trends). Top panel: the β -spectrum for a composition with $Y_{e,0} = 0.25$. The spectrum is shifted to higher energies relative to the low- $Y_{e,0}$ case (Figure 3). Bottom panels: the fraction of Q_β , χ , imparted to β -particles, γ -rays, and neutrinos for different values of $Y_{e,0}$. As $Y_{e,0}$ increases, a greater fraction of Q_β goes to β 's and neutrinos, while χ_γ shrinks. This effect is particularly pronounced at late times.

mildly on electron fraction, with higher $Y_{e,0}$ slightly enhancing the spectrum's high-energy tail.

This is due to differences in how β -decay energy is divided among β -particles, γ -rays, and neutrinos. Compositions evolved from higher initial Y_e impart a greater *fraction* of the total β -decay energy Q_β to β -particles at the expense of γ -rays (see the lower three panels of Figure 4). As shown in Figure 1, higher electron fractions yield compositions with lower A . The β -decays for these lighter nuclei tend to be dominated by one or a few transitions to low-lying nuclear energy states; the energy carried away by the β -particle and the neutrino is close to Q_β , and the energy released in γ -rays during nuclear de-excitation is reduced. In contrast, for more massive nuclei, the excitation energy of the daughter nucleus after emission of the β -particle and neutrino is more likely to be a significant fraction of Q_β , and a greater portion of the energy takes the form of γ -rays. Therefore, despite having similar Q_β , nuclei

synthesized in high- $Y_{e,0}$ conditions generate more energetic β -particles. We found these effects to be independent of mass model.

2.5.2. α -Decay

While the majority of species produced by the r -process stabilize through β -decay, some heavier isotopes ($A \gtrsim 200$) undergo α -decay. Unlike β -particles, α -particles are ejected from nuclei at discrete energies that fall within the fairly narrow range $E_\alpha \sim 5\text{--}9$ MeV. Due to the fact that α -decay is a tunneling process, α -particles carry all of the decay energy in the majority of decays, and the incidence of γ -emission is vanishingly low.

We determined the most important sources of α -emission using the procedure detailed above for β -decays. The α -spectrum as a function of time is given in the bottom panel of Figure 3. The energy is fairly evenly distributed in the range 5 MeV $< E_\alpha <$ 9 MeV.

2.5.3. Fission

Spontaneous, neutron-induced, and β -delayed fission of heavy nuclei ($A \gtrsim 250$) contribute a few percent of the total r -process radioactive decay energy at times $\lesssim 1$ day. The mass distribution and energy spectra of the fission fragments depend sensitively on the nuclear physics models, and a thorough exploration of these parameters is beyond the scope of this work. We can, however, estimate the final kinetic energy of fission as equal to the repulsive Coulomb energy between the daughter nuclei immediately after fission occurs:

$$E_{K,\text{tot}} = E_{\text{Coul}} = \frac{Z_1 Z_2 e^2}{r_0 (A_1^{1/3} + A_2^{1/3})}, \quad (3)$$

where e is the elementary charge, (A_1, Z_1) and (A_2, Z_2) are the masses and atomic numbers of the daughter nuclei, and the nuclear radius is given by $r_0 A^{1/3}$. For deformed post-scission nuclei, $r_0 \simeq 1.8$ fm.

Fission favors the production of nuclei at or near the doubly magic nucleus $(A, Z) = (132, 50)$. Assuming a typical parent isotope has mass and atomic numbers $A_p = 250$ and $Z_p = 100$, and that $(A_1, Z_1) = (132, 50)$, the fission daughters will have kinetic energies of order 100 MeV. We assume the fission fragment spectrum is flat, and ranges from 100 to 150 MeV. Given the limited role of fission at times later than one day, a more detailed treatment is unnecessary.

3. THERMALIZATION PHYSICS

In this section, we discuss the processes by which energetic decay products thermalize in the kilonova ejecta, and present energy-loss rates for β -particles, α -particles, and fission fragments.

3.1. γ -rays

γ -rays lose energy through photoionization and Compton scattering. We calculated the Compton opacity from the Klein-Nishina formula and the photoionization opacity using the Photon Cross Section Database (XCOM; Berger et al. 2010) published by the National Institute of Standards and Technology (NIST).

The total γ -ray opacity for our fiducial composition at $t = 1$ day is shown in Figure 5. The high-Z elements produced in the

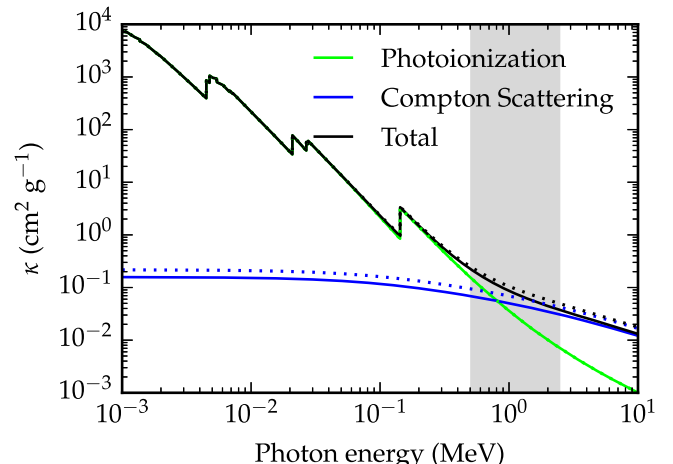


Figure 5. γ -ray opacity, κ , in the inner (solid lines) and outer (dotted lines) ejecta. Photoionization opacity is plotted in green, Compton opacity in blue, and total opacity in black. Differences between the inner and outer ejecta compositions have a negligible impact on κ . The gray bar indicates the energies at which most γ -rays are emitted.

r -process have higher ionization thresholds (~ 100 keV) than do the metals in typical astrophysical mixtures, so the photoionization cross section in kilonovae dominates out to ~ 1 MeV, above which Compton scattering takes over. The opacity varies little between the inner and outer ejecta, and changes over time are minor, so we assume the γ -ray opacity to be constant.

Both photoionization and Compton scattering events produce a non-thermal electron, which loses energy by the physical processes described in the next section.

3.2. γ -particles

Suprathermal β -particles lose energy primarily through Coulomb interactions with free thermal electrons (plasma losses), and by exciting or ionizing bound atomic electrons. Bremsstrahlung (free-free) emission is important for very high-energy β -particles. While earlier studies of thermalization assumed plasma interactions dominated the energy loss, we find β -particles lose most of their energy to ionization and excitation.

In the limit that the β -particle energy far exceeds that of thermal electrons, the plasma energy loss per unit time is (Huba 2013)

$$\dot{E}_\beta^{\text{pl}} = 7.7 \times 10^{-15} E_\beta^{-1/2}$$

$$\times \left(\frac{n_e}{1 \text{ cm}^{-3}} \right) \lambda_{ee} \left(1.0 - \frac{3.9}{7.7} \frac{T}{E_\beta} \right) \text{ MeV s}^{-1}, \quad (4)$$

where E_β is the β -particle's kinetic energy in MeV, T is the ejecta temperature in MeV, $\lambda_{ee} \sim 10$ is the Coulomb logarithm for electron-electron scattering, and n_e is the free electron number density. Radioactive β -particles have $E_\beta \sim 1$ MeV, whereas $k_B T \sim 1$ eV in kilonova ejecta, so the assumption that $E_\beta \gg k_B T$ holds. We determine n_e assuming that all elements heavier than hydrogen are singly ionized, as expected for kilonova ejecta near peak brightness (Kasen et al. 2013). The outer ejecta contains a substantial quantity of hydrogen, which

we assume to be neutral given the low temperatures ($T \lesssim 5000$ K) expected in the ejecta periphery.

We calculate energy losses due to ionization and excitation of atomic electrons using the well established formula (Heitler 1954; Berger & Seltzer 1964; Blumenthal & Gould 1970; Gould 1975; see also Chan & Lingenfelter 1993 and Milne et al. 1999)

$$\dot{E}_\beta^{\text{IE}} = \frac{2\pi r_e^2 m_e c^3 n_{e,b}}{v_\beta/c} \times \left\{ 2 \ln\left(\frac{E_\beta}{\bar{I}}\right) + \ln\left(1 + \frac{\tau}{2}\right) + \left(1 - \frac{v_\beta^2}{c^2}\right) g(\tau) \right\}, \quad (5)$$

$$g(\tau) = 1 + \frac{\tau^2}{8} - (2\tau + 1)\ln 2, \quad (6)$$

where r_e is the classical electron radius, m_e is the electron mass, $n_{e,b}$ is the number density of bound electrons, v_β is the β -particle's speed, and $\tau = E_\beta/m_e c^2$. The quantity \bar{I} is an average ionization and excitation potential which can be approximated for an element of atomic number Z as (Segré 1977)

$$\bar{I} = 9.1Z\left(1 + \frac{1.9}{Z^{2/3}}\right) \text{ eV}. \quad (7)$$

Following Chan & Lingenfelter (1993), we use averaged quantities for $n_{e,b}$ and \bar{I} ,

$$\langle n_{e,b} \rangle = \frac{\rho}{m_u} \left\langle \frac{Z}{A} \right\rangle, \quad (8)$$

$$\left\langle \ln \frac{\bar{I}}{\text{eV}} \right\rangle = \left\langle \frac{Z}{A} \right\rangle^{-1} \sum_j \left(\frac{Z}{A} \right)_j X_j \ln \left(\frac{\bar{I}_j}{\text{eV}} \right), \quad (9)$$

where

$$\left\langle \frac{Z}{A} \right\rangle = \sum_j \left(\frac{Z}{A} \right)_j X_j, \quad (10)$$

m_u is the nuclear mass unit, X_j is the mass fraction of element j , and the sum runs over all species in the composition. For the inner (outer) ejecta, we find $\langle \ln \bar{I}/\text{eV} \rangle = 6.4$ (4.9), and $\langle Z/A \rangle = 0.4$ (0.55).

Plasma and ionization/excitation losses are the cumulative results of many distant interactions that individually transfer very little energy. The thermal and bound electrons energized by β -particles through these channels have very low kinetic energies and thermalize rapidly. Instead of tracking secondary electrons explicitly, we assume their kinetic energy is transferred directly to the thermal pool.

Bremsstrahlung (free-free) and synchrotron emission are other possible means of β -particle energy loss. The rate of cooling due to synchrotron emission in a magnetic field B is

$$\dot{E}_\beta^{\text{syn}} = \frac{4}{9} r_e^2 c \gamma^2 \left(\frac{v_\beta}{c} \right)^2 B^2, \quad (11)$$

where γ is the β -particle's Lorentz factor. Neglecting logarithmic terms (which only increase $\dot{E}_\beta^{\text{IE}}$), and assuming $\langle Z/A \rangle = 0.4$ and $\gamma^2(v_\beta/c)^3 \approx 10$, we estimate the ratio of

synchrotron to ionization/excitation losses as

$$\frac{\dot{E}_\beta^{\text{syn}}}{\dot{E}_\beta^{\text{IE}}} \sim 1.6 \times 10^{-15} \left(\frac{B_d}{3.7 \times 10^{-6} \text{ G}} \right)^2 M_5^{-1} v_2^{-1} t_d^{-1}, \quad (12)$$

where $M_5 = M_{\text{ej}}/(5 \times 10^{-3} M_\odot)$ and B_d is the magnetic field at one day. This is much less than unity for all parameters of interest, so we neglect synchrotron losses.

In contrast, Bremsstrahlung contributes, albeit modestly, to β energy loss for $E_\beta \gtrsim 1$ MeV. From Seltzer & Berger (1986),

$$\dot{E}_\beta^{\text{Brem}} = n_i v_\beta (E_\beta + m_e c^2) Z^2 r_0^2 \alpha \phi_{\text{rad}}, \quad (13)$$

where n_i is the number density of the scattering species, α is the fine-structure constant, and ϕ_{rad} are energy-dependent empirical fitting constants, also from Seltzer & Berger (1986). We model Bremsstrahlung losses in the inner ejecta using characteristic values $Z = 60$ and $A = 144$, similar to the average values of the inner composition. For the outer ejecta, we use a two-component composition, with $(Z, A) = (1, 1)$ accounting for the high amount of hydrogen, and $(Z, A) = (55, 133)$ representing elements with $Z > 1$.

Bremsstrahlung may produce high-energy photons that do not thermalize promptly in the ejecta, an effect of the order of $\lesssim 10\%$ at typical β -particle energies. Our treatment of Bremsstrahlung is discussed in more detail in Appendix A.3.

We plot the total energy-loss rate in the inner and outer ejecta, normalized to mass density, in the top panel of Figure 6. While the lower degree of ionization in the outer ejecta makes plasma and Bremsstrahlung losses less efficient, this is more than compensated for by enhanced ionization and excitation losses due to the greater number of bound electrons per nucleon, and to the lower average ionization potential. Overall, thermalization rates in the outer ejecta are higher by a factor of a few.

3.3. α -particles

Suprathermal α -particles thermalize by interacting with free and bound electrons. Long-range interactions with ions and short-range interactions with atomic nuclei do not significantly contribute to α -particle energy loss.

α -particles scattering off of free, thermal electrons lose energy at the rate given by Huba (2013) for fast ions in a plasma,

$$\dot{E}_i^{\text{pl}} = 1.7 \times 10^{-13} E_i^{-1/2} \mu_i^{1/2} Z_i^2 \left(\frac{n_e}{1 \text{ cm}^{-3}} \right) \lambda_{ie} \times \left(2 - \frac{1.1 \times 10^{-3}}{\mu_i} - \frac{T}{E_i} \right) \text{ MeV s}^{-1}, \quad (14)$$

where E_i is the ion's kinetic energy in MeV, μ_i is the ion mass in m_u , Z_i is the charge in units of the elementary charge, and $\lambda_{ie} \sim 5\text{--}10$ is the Coulomb logarithm for ion-electron scattering. For α -particles, $Z_i = 2$ and $\mu_i = 4$.

The rates of α -particle energy loss due to interactions with bound electrons are taken from NIST's ASTAR database (Berger et al. 2005). Lacking α -particle stopping powers for all elements in our r -process mixture, we map the full inner and outer compositions onto a reduced set of elements for which α -stopping data are available (see Figure 7). The middle panel of Figure 6 shows the total α -particle energy-loss rates. Plasma

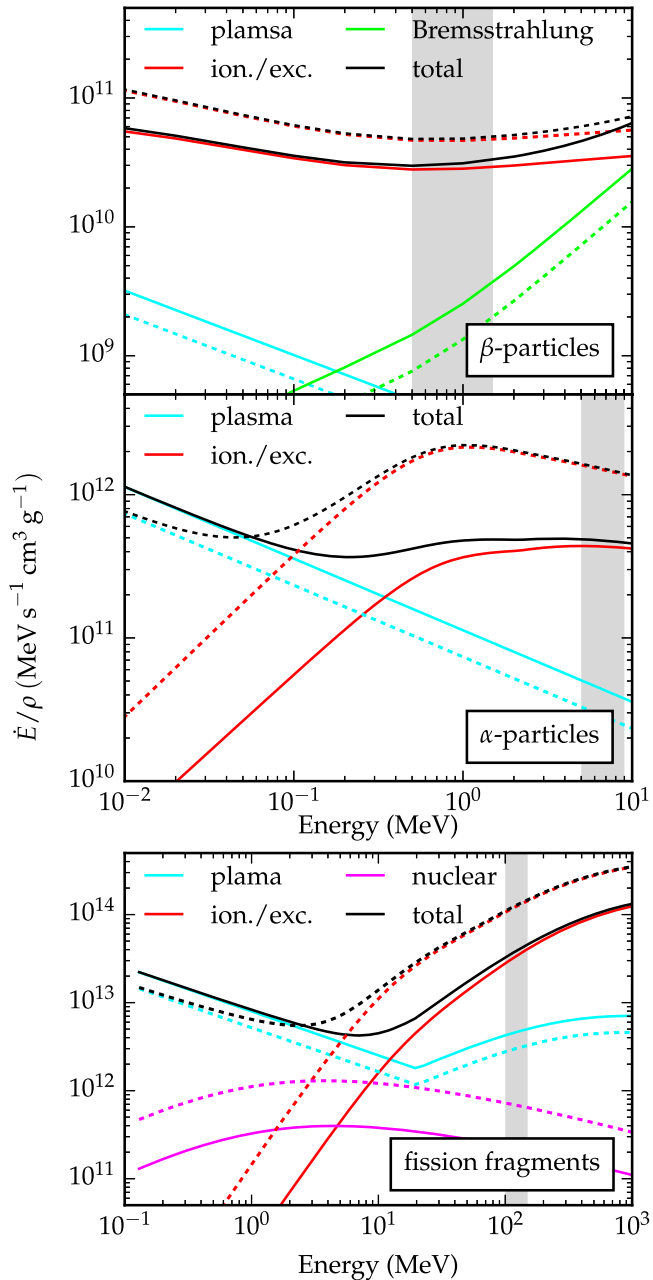


Figure 6. All panels: energy-loss rates in the inner (outer) ejecta are plotted in solid (dashed) lines. Gray bars indicate typical particle energies at emission. Top panel: the total energy-loss rate for fast β -particles, normalized to the mass density ρ . Thermalization rates are higher in the outer ejecta by a factor of a few. Middle panel: the energy-loss rates for α -particles in simplified r -process mixtures standing in for the full inner and outer ejecta compositions (see Figure 7), normalized to density. Alpha particle thermalization is a few to $\sim 10 \times$ more efficient in the outer ejecta. Bottom panel: the energy-loss rate for fission fragments, normalized to density and assuming most atoms in the ejecta are singly ionized. Thermalization is more efficient in the outer ejecta.

losses dominate for $E_\alpha \lesssim 1$ MeV, while interactions with bound electrons are important at higher energies. The thermalization rate in the outer ejecta is greater than in the inner ejecta by up to an order of magnitude.

3.4. Fission Fragments

Interactions with free and bound electrons and with atomic nuclei all contribute to fission fragment thermalization. The

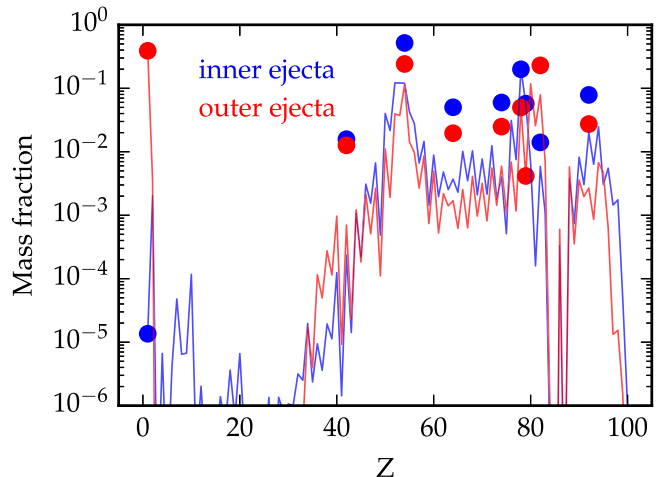


Figure 7. Simplified composition (circles) used to calculate the electronic stopping for α -particles and fission fragments. The full compositions, shown in solid lines, were mapped onto a composition of elements for which α -particle and proton stopping data were available through NIST's ASTAR database.

energy loss to thermal free electrons is described by Equation (14), where Z_i depends on the ionization state of the fission fragment and the length scale of the collision. For impact parameters greater than the size of the interacting particles, the relevant charge is the total charge carried by the fragment, $Z_{ff,ion} = Z_{nuc} - N_{e,b}$, where Z_{nuc} is the fragment's atomic number and $N_{e,b}$ is the number of bound electrons. At lower impact parameters, more of the nuclear charge is felt.

We calculate $Z_{ff,ion}$ as a function of fission fragment energy E_{ff} using the formula of Schiavietz & Grande (2001) for the ion charge state in a gaseous medium. Since fragments with $Z_{ff,ion} \gtrsim 7$ deflect thermal electrons at impact parameters greater than the fission fragment radius, we set $Z_i \rightarrow \max\{Z_{ff,ion}(E_{ff}), 7\}$. Fission fragments can scatter off thermal ions at much lower impact parameters, in which case the full nuclear charge is felt. The energy loss from these interactions is given by the nuclear stopping formula of Ziegler (1980).

To model the stopping of heavy particles by bound electrons, we adopt the technique of Ziegler (1980), in which the stopping power of a heavy particle in any material is proportional to the stopping power of a proton in the same material, with the constant of proportionality given by $Z_{ff,ion}^2$. We calculate the stopping power for the same simplified composition used to model α -particle energy loss, using proton stopping powers extracted from NIST's PSTAR database (Berger et al. 2005).

The total energy-loss rate for fission fragments is presented in the bottom panel of Figure 6. Interactions with bound electrons dominate the rate at high energies, while losses to free electrons become important at energies less than ~ 10 MeV. Thermalization rates in the outer composition are a factor of a few higher than in the inner composition.

4. ANALYTIC RESULTS

Before moving to detailed numerical calculations of kilonova thermalization, we consider simple analytic estimates of the relevant timescales and time evolution. This work extends the analytic treatments proposed by Metzger et al. (2010) and Hotokezaka et al. (2016). Unless stated otherwise, our estimates describe thermalization in the “inner” composition, which typically makes up $\sim 90\%$ or more of the ejected mass.

4.1. Analytic Estimates of Thermalization Timescales

The net thermalization of the energy from the radioactive decay of r -process material depends on the relative importance of each decay channel and on how efficiently the decay products thermalize in the ejecta. Energy-loss rates depend on the density of the medium, so thermalization is also a function of M_{ej} and v_{ej} . If we approximate the ejecta as a uniform density sphere of mass M_{ej} and kinetic energy $E_{\text{k}} = M_{\text{ej}}v_{\text{ej}}^2/2$, the density is

$$\rho(t) \approx 7.9 \times 10^{-15} M_5 v_2^{-3} t_{\text{d}}^{-3} \text{ g cm}^{-3}, \quad (15)$$

where again, $M_5 = M_{\text{ej}}/5.0 \times 10^{-3} M_{\odot}$ and $v_2 = v_{\text{ej}}/0.2c$. Thermalization becomes inefficient at a time, t_{ineff} , when the timescale for a particle to thermalize becomes similar to the ejecta expansion timescale, t_{exp} . The inefficiency time can be compared to the peak of the kilonova light curve,

$$t_{\text{peak}} \sim \left(A \frac{M_{\text{ej}} \kappa}{v_{\text{ej}} c} \right)^{1/2} \simeq 4.3 M_5^{1/2} v_2^{-1/2} \text{ days}, \quad (16)$$

where κ is the opacity for optical/infrared light (we take $\kappa = 10 \text{ cm}^2 \text{ g}^{-1}$, appropriate for an r -process medium), and $A = 0.32$ is a scaling factor we estimate from kilonova radiation transport simulations (e.g., Barnes & Kasen 2013). If $t_{\text{ineff}} < t_{\text{peak}}$, thermalization will impact the kilonova light curve significantly.

γ -rays: γ -rays stop thermalizing efficiently when they can escape the ejecta without undergoing any scatters or absorptions. This occurs when the optical depth $\tau \approx \rho \kappa_{\gamma} R_{\text{ej}}$ falls below unity. For γ -rays with energies $E_{\gamma} \gtrsim 1 \text{ MeV}$, the relevant opacity is the Compton opacity, $\kappa_{\text{C}} \approx 5 \times 10^{-2} \text{ cm}^2 \text{ g}^{-1}$ while the photoionization opacity, $\kappa_{\text{PI}} \gtrsim 1 \text{ cm}^2 \text{ g}^{-1}$, dominates for lower energy photons. The ejecta becomes transparent ($\tau < 1$) to γ -rays at a time

$$t_{\text{ineff}} \approx \begin{cases} 0.5 M_5^{1/2} v_2^{-1} \text{ days} & \text{for } E_{\gamma} \gtrsim 1 \text{ MeV} \\ 2.3 M_5^{1/2} v_2^{-1} \text{ days} & \text{for } E_{\gamma} \lesssim 1 \text{ MeV}. \end{cases} \quad (17)$$

In both cases, inefficiency sets in before the kilonova light curve peaks,

$$\frac{t_{\text{ineff}}}{t_{\text{peak}}} \approx \begin{cases} 0.12 v_2^{-1/2} & E_{\gamma} \gtrsim 1 \text{ MeV} \\ 0.5 v_2^{-1/2} & E_{\gamma} \lesssim 1 \text{ MeV}. \end{cases} \quad (18)$$

β -particles: The energy-loss rate for β -particles, modulo mass density, has a fairly constant value $\dot{E}_{\beta} \simeq 4 \times 10^{10} \rho \text{ MeV s}^{-1}$ over a broad range of energies (see Figure 6). The thermalization time for β -particles is

$$\begin{aligned} t_{\text{th}} &\approx \frac{E_{\beta,0}}{\dot{E}_{\beta,0}} = \frac{E_{\beta,0}}{4 \times 10^{10} \rho \text{ MeV s}^{-1}} \\ &= 0.02 \left(\frac{E_{\beta,0}}{0.5 \text{ MeV}} \right) M_5^{-1} v_2^3 t_{\text{d}}^3 \text{ days}, \end{aligned} \quad (19)$$

where $E_{\beta,0}$ is the initial β -particle energy.

Beta particles trapped in the ejecta fail to efficiently thermalize when $t_{\text{th}} \gtrsim t_{\text{exp}}$, which occurs at

$$t_{\text{ineff}} \approx 7.4 \left(\frac{E_{\beta,0}}{0.5 \text{ MeV}} \right)^{-1/2} M_5^{1/2} v_2^{-3/2} \text{ days}. \quad (20)$$

For a typical initial energy, t_{ineff} is comparable to the rise time of the light curve,

$$\frac{t_{\text{ineff}}}{t_{\text{peak}}} \approx 1.7 \left(\frac{E_{\beta,0}}{0.5 \text{ MeV}} \right)^{-1/2} v_2^{-1}. \quad (21)$$

If the magnetic field is radial or only slightly tangled, β -particles can escape the ejecta before they thermalize, and escape will significantly reduce the thermalization efficiency. The escape time is

$$t_{\text{esc}} \simeq \frac{R_{\text{ej}}(t)}{\lambda v_{\beta,\parallel}}, \quad (22)$$

where λR_{ej} is the coherence length of the magnetic field, $v_{\beta,\parallel}$ is the component of the β -particle velocity parallel to the field lines, and we have modeled the β 's motion in a random field as a random walk of step size λR_{ej} . For a β -particle with $E_{\beta,0} = 0.5 \text{ MeV}$ and pitch angle 1 ($v_{\beta,\parallel} = v_{\beta}$), t_{esc} is less than t_{th} when

$$t \gtrsim \frac{3.5 M_5^{1/2} v_2^{-1}}{\lambda^{1/2}} \text{ days}. \quad (23)$$

For radial fields ($\lambda = 1$), this is less than t_{peak} , so escape is important for β -particle thermalization. In contrast, for disordered fields there is a degree of randomness above which β -particle escape cannot significantly impact the light curve. This limit is defined by the condition $t_{\text{th}}(t_{\text{peak}}) < t_{\text{esc}}(t_{\text{peak}})$. Again considering a 0.5 MeV β -particle, we find

$$t_{\text{th}}(t_{\text{peak}}) < t_{\text{esc}}(t_{\text{peak}}) \rightarrow \lambda \lesssim 0.8 v_2^{-1}. \quad (24)$$

Thus, high-energy β -particles are effectively trapped by even a slightly tangled magnetic field.

α -particles and fission fragments: Fission fragments and α -particles are emitted with greater energies than β -particles ($E_{\alpha,0} \simeq 6 \text{ MeV}; E_{\text{ff},0} \simeq 100 \text{ MeV}$), but have higher energy-loss rates ($\dot{E}_{\alpha}(E_{\alpha,0}) \sim 5 \times 10^{11} \rho \text{ MeV s}^{-1}$; $\dot{E}_{\text{ff}}(E_{\text{ff},0}) \sim 5 \times 10^{13} \rho \text{ MeV s}^{-1}$). The efficiency of α -particle thermalization is similar to that of β particles, while fission fragments thermalize efficiently out to very late times:

$$\frac{t_{\text{ineff}}}{t_{\text{peak}}} \approx \begin{cases} 1.8 \left(\frac{E_{\alpha,0}}{6 \text{ MeV}} \right)^{-1/2} v_2^{-1} & \alpha\text{-particles} \\ 3.9 \left(\frac{E_{\text{ff},0}}{125 \text{ MeV}} \right)^{-1/2} v_2^{-1} & \text{fiss. fragments}. \end{cases} \quad (25)$$

Unlike β -particles, both α 's and fission fragments have velocities much lower than v_{ej} , and so in general cannot escape the ejecta. However, because these particles are propagating through a steep velocity gradient, their speed relative to the background gas continually decreases. This reduces the kinetic energy of the particles as measured in the co-moving frame. Because the particles have a spiraling motion about magnetic field lines, their motion is never completely frozen out in the fluid frame. Still, these “frame-to-frame” effects can reduce thermalization by $\lesssim 15\%$.

4.2. Summary of Thermalization Timescales

While low-energy β -particles, α -particles, and especially fission fragments typically thermalize efficiently at $t = t_{\text{peak}}$,

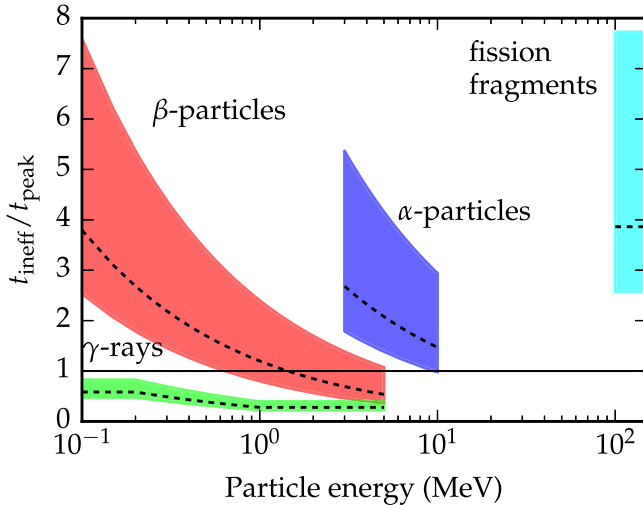


Figure 8. Ratio $t_{\text{ineff}}/t_{\text{peak}}$ for all particles, for v_{ej} in the range $0.1c$ – $0.3c$. Fission fragments, and to a lesser extent α -particles and low-energy β -particles, thermalize efficiently out to late times. Higher energy β 's and γ -rays are expected to become inefficient on kilonova timescales. The width of the curves is due to the range of v_{ej} considered, since $t_{\text{ineff}}/t_{\text{peak}}$ varies inversely with v_{ej} . Curves for the fiducial velocity $v_{\text{ej}} = 0.2c$ are overplotted in dotted black lines.

the thermalization at peak of high-energy β -particles and γ -rays is not robust. Figure 8 plots the ratio of the thermalization time to the light curve peak for all particles as a function of initial energy for a range of v_{ej} . For α - and β -particles, we calculated $t_{\text{ineff}}/t_{\text{peak}}$ from Equations (25) and (21). The γ -ray curve was calculated from Equation (18) for $E_\gamma \leq 200$ keV, (18) for $E_\gamma \geq 1$ MeV, and a simple linear interpolation for intermediate E_γ . For fission fragments, we modified Equation (25) slightly to account for the positive slope of \dot{E}_{ff} in the range $E_{\text{ff}} = 100$ – 150 MeV. This renders \dot{E}_{ff} approximately constant, so the fission fragment curve is essentially flat.

4.3. Analytic Thermalization Model

We develop an analytic expression for time-dependent thermalization efficiencies of massive particles under the following assumptions: first, that the radioactive energy-generation rate evolves as $t^{-\eta}$ with $\eta = 1.0$ (close to the expected values $\eta = 1.1$ – 1.4); second, that the density in the ejecta is spatially uniform; third, that energy-loss rates are independent of particle energy, and depend only on ρ ; and fourth, that all particles of a given type are emitted at a single energy E_0 . Despite these simplifications, we find our model agrees fairly well with the detailed numerical calculations to be presented in Section 5.

The thermalization efficiency is defined as the ratio of energy emitted by radioactive processes to energy absorbed by the ejecta at any time t ,

$$f(t) = \frac{\dot{E}_{\text{th}}(t)}{\dot{E}_{\text{rad}}(t)}. \quad (26)$$

We approximate the radioactive energy-generation rate by $\dot{E}_{\text{rad}} = \dot{\epsilon}_0(t_0/t)$ with $\dot{\epsilon}_0 = 10^{11} M_{\text{ej}} \text{ ergs s}^{-1}$ and $t_0 = 1$ day. Assuming charged particle thermalization depends only on mass density (which declines like t^{-3} in a homologous flow),

the energy loss is

$$\dot{E}_{\text{part}}(t) = \psi \rho_0 \left(\frac{t}{t_0} \right)^{-3}, \quad (27)$$

where ρ_0 is the density at t_0 , and ψ is a scaling factor such that $\psi \rho_0 = \dot{E}_{\text{part}}(t_0)$, which will be unique to each particle type. The rate at which energy is thermalized, $\dot{E}_{\text{th}}(t)$, is given by the number of live particles N multiplied by the rate at which they lose energy,

$$\dot{E}_{\text{th}}(t) = N(t) \times \psi \rho_0 \left(\frac{t}{t_0} \right)^{-3}. \quad (28)$$

At any time t , the oldest live particle originates from an earlier time t_i , defined by

$$E_{\text{part}}(t) = E_0 - \int_{t_i}^t \psi \rho_0 \left(\frac{t'}{t_0} \right)^{-3} dt' = 0, \quad (29)$$

which is satisfied by

$$t_i = \left(\frac{\psi \rho_0 t_0^3 t^2}{2E_0 t^2 + \psi \rho_0 t_0^3} \right)^{1/2}. \quad (30)$$

The number of live particles at time t is then

$$N(t) = \frac{\dot{\epsilon}_0 t_0}{2E_0} \ln \left[1 + 2 \left(\frac{t}{t_{\text{ineff}}} \right)^2 \right] \quad (31)$$

where t_{ineff} is the inefficiency timescale defined in the previous section.

It is now straightforward to calculate the ratio f_p of thermalized to emitted energy for a massive particle of type p ,

$$f_p(t) = \frac{\dot{E}_{\text{th}}}{\dot{E}_{\text{rad}}} = \frac{\ln \left[1 + 2 \left(\frac{t}{t_{\text{ineff},p}} \right)^2 \right]}{2 \left(\frac{t}{t_{\text{ineff},p}} \right)^2}. \quad (32)$$

Equation (32) can be used to estimate the thermalization efficiencies of massive particles, where the relevant timescales $t_{\text{ineff},p}$ are given by Equations (21) (β -particles), (25) (α -particles), and (25) (fission fragments).

For γ -rays, the thermalization efficiency is approximately equal to the interaction probability: $f_\gamma(t) \approx 1 - e^{-\tau}$. We can estimate the optical depth $\tau \approx \rho \kappa_\gamma R_{\text{ej}}$ using $\bar{\kappa}_\gamma$, the γ -ray opacity averaged over the emission spectrum. Optical depth is related to $t_{\text{ineff},\gamma}$ by

$$\begin{aligned} \left(\frac{t_{\text{ineff},\gamma}}{t_0} \right)^2 &= \rho_0 \bar{\kappa}_\gamma R_0 = \tau_0 \\ \rightarrow \tau(t) &= \tau_0 \left(\frac{t}{t_0} \right)^{-2} = \left(\frac{t_{\text{ineff},\gamma}}{t} \right)^2, \end{aligned}$$

so

$$f_\gamma(t) = 1 - \exp \left[- \left(\frac{t}{t_{\text{ineff},\gamma}} \right)^2 \right]. \quad (33)$$

Figure 9 shows our analytic thermalization functions for $M_{\text{ej}} = 5 \times 10^{-3} M_\odot$, and $v_{\text{ej}} = 0.2c$, using the expressions for t_{ineff} derived in Section 3. For massive particles, we used

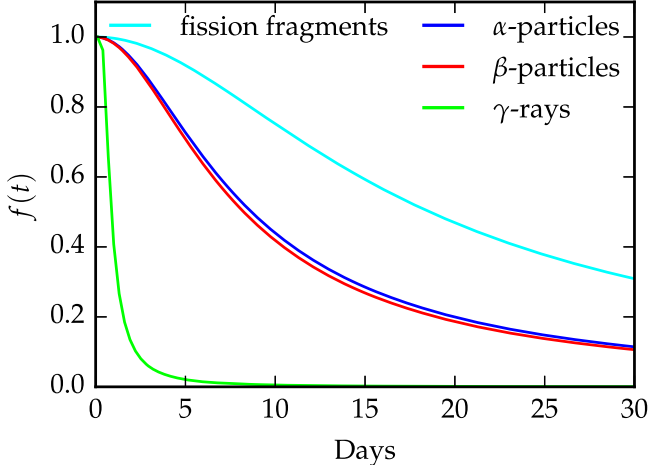


Figure 9. Analytic thermalization efficiencies calculated with Equations (32) and (33). We use $t_0 = 1$ day, and $\rho_0 = 7.9 \times 10^{-15} \text{ cm}^{-3}$, corresponding to a uniform density ejecta with the same mass and energy as our fiducial model. For α 's, β 's, and fission fragments we take $E_0 = 6, 1$, and 125 MeV , respectively.

$E_{\beta,0} = 0.5 \text{ MeV}$, $E_{\alpha,0} = 6 \text{ MeV}$, and $E_{ff,0} = 125 \text{ MeV}$. For γ -rays, we take $\bar{\kappa} = 0.1 \text{ cm}^2 \text{ g}^{-1}$, which gives $t_{\text{ineff},\gamma} \approx 1.4$ days.

As we will see in Section 5, the approximate analytic expressions Equations (32) and (33) agree fairly well with our numerical results.

5. NUMERICAL RESULTS

In this section, we present numerical calculations of thermalization efficiencies as determined by modeling the three-dimensional (3D) transport of γ -rays, fission fragments, and α - and β -particles in a magnetized expanding medium. Our calculations used the time-evolving emission spectra introduced in Section 2.5, accounted for the time-dependent partition of radioactive energy among different decay products, and incorporated the detailed, energy-dependent energy-loss rates derived in Section 3. The flux tube approximation was used to model charged particle transport, allowing us to explore the sensitivity of our results to the architecture of the ejecta's magnetic field. Additional details of our transport method are given in the Appendix.

5.1. Thermalization Efficiencies

Figure 10 presents the numerically calculated thermalization efficiency, $f(t)$, of all particles for the fiducial ejecta model ($M_{\text{ej}} = 5 \times 10^{-3} M_{\odot}$ and $v_{\text{ej}} = 0.2c$.) Fission fragments thermalize most efficiently, having $f(t) \gtrsim 0.5$ out to $t \sim 15$ days. α - and β -particle thermalization is slightly lower, reaching $f(t) = 0.5$ around a week post-merger, while $f(t)$ for γ -rays is much lower, falling below 0.5 by $t \sim 1$ day.

For massive particles, we show $f(t)$ for radial (dotted lines), toroidal (solid lines), and lightly tangled ($\lambda = 0.25$; dashed lines) magnetic field geometries. The magnetic field configuration affects thermalization in three ways.

1. *Diffusion:* Radial or lightly tangled fields allow particles to diffuse outward into regions of lower density, and lead to lower $f(t)$.

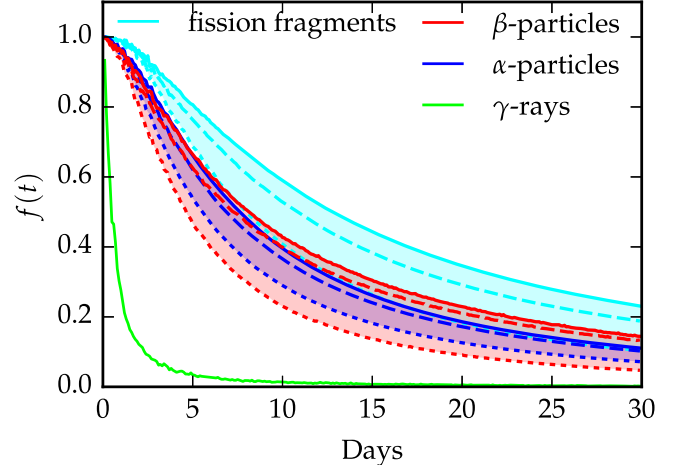


Figure 10. Thermalization efficiencies $f(t)$ for all particles in an ejecta with $M_{\text{ej}} = 5 \times 10^{-3} M_{\odot}$ and $v_{\text{ej}} = 0.2c$ (our fiducial model). Fission fragments thermalize most efficiently, followed by α -particles, β -particles, and γ -rays. For charged particles, we plot $f(t)$ for radial (dotted lines), toroidal (solid lines), and moderately tangled ($\lambda = 0.25$; dashed lines) magnetic fields. Toroidal fields thermalize most efficiently, followed by random, then radial fields.

2. *Escape:* Radial fields that allow charged particles to escape before they have completely thermalized will lower $f(t)$. This is most important for β -particles, which move faster than the ejecta.
3. *Frame-to-frame effects:* Particles in a homologous flow lose energy, as measured in the co-moving frame (cmf), as they move through the ejecta. These frame-to-frame losses reduce the amount of kinetic energy a particle has to thermalize, and therefore reduce $f(t)$. Radial fields and lightly tangled fields, which allow particles to move fairly freely through the ejecta, facilitate frame-to-frame effects. These losses are most important for α -particles and fission fragments, which have velocities of the order of v_{ej} , and thus have substantially different cmf energies in different regions of the ejecta.

In light of the above, it is not surprising that toroidal fields maximize $f(t)$; toroidal fields hold particles at one position in velocity space, preventing diffusion, escape, and frame-to-frame losses. Radial fields, in contrast, enhance all three of these effects and hence minimize $f(t)$. Thermalization in random fields falls between these two extremes. This behavior holds for all ejecta models studied.

While the trends shown in Figure 10—i.e., that $f_{ff}(t) > f_{\alpha}(t) \approx f_{\beta}(t) > f_{\gamma}(t)$ —are consistent across ejecta models, the values of $f(t)$ can vary significantly with M_{ej} and v_{ej} . Figure 11 illustrates the variance and clarifies the dependence of $f(t)$ on the ejecta parameters. For each point ($M_{\text{ej}}, v_{\text{ej}}$) in parameter space, and for each particle type, we plot t_{50} —the time at which $f(t)$ drops to 50%. (Cases in which $f(t = 30 \text{ days}) > 50\%$ are omitted from Figure 11.) To show how sensitive thermalization is to magnetic fields, we include results for radial (top panel) and toroidal (bottom panel) field geometries.

The thermalization of all particles increases with M_{ej} and decreases with v_{ej} . The changes in efficiency are especially dramatic for massive particles. For the heaviest ejecta mass considered ($M_{\text{ej}} = 5 \times 10^{-2} M_{\odot}$), massive particles thermalize

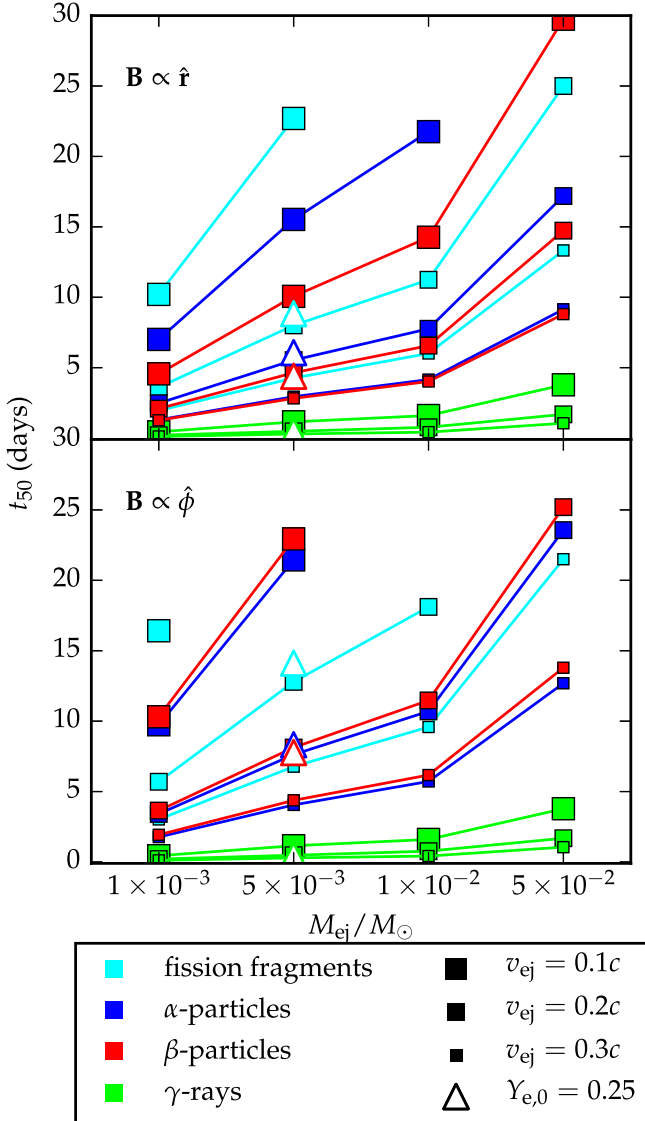


Figure 11. Time at which $f(t)$ drops below 50% (t_{50}) for all particles for all M_{ej} and v_{ej} considered. Results for a radial (toroidal) magnetic field are shown in the top (bottom) panel. Thermalization increases with mass and decreases with velocity. Fission fragments thermalize most efficiently, followed by α -particles and β -particles, and finally γ -rays. Toroidal fields result in more robust thermalization of all massive particles.

efficiently out to late times regardless of v_{ej} . The thermalization of γ -ray energy is low for all models tested.

Though the results shown are for the two-component composition described above, we find that the higher energy-loss rates in the outer ejecta have only a small impact on thermalization. For radial fields, where the effect is most pronounced, the two-zone model results in an increase in total thermalization of <5% relative to a one-zone model that assumes the entire ejecta has the “inner” ejecta composition. The $f(t)$ we calculate should be fairly insensitive to the exact division between inner and outer ejecta.

5.1.1. Effect of Aspherical Ejecta

The ejecta from a CO merger is likely to be aspherical, particularly in the case of an NSBH merger, where most of the ejected mass is confined to the equatorial plane (e.g.,

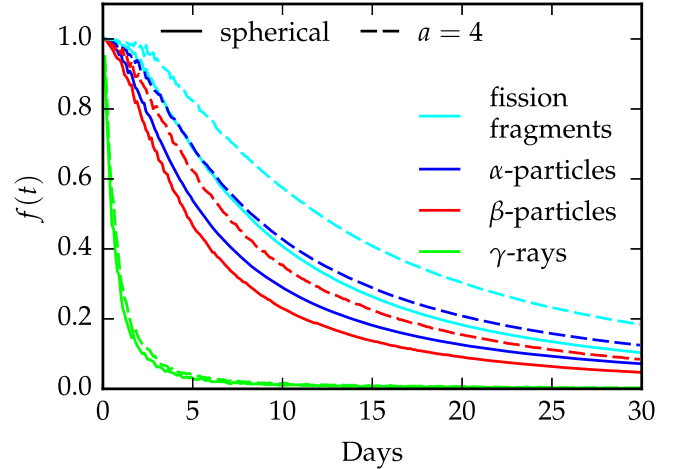


Figure 12. Thermalization efficiencies for oblate ejecta with aspect ratio $a = 4$, compared to the standard spherical geometry, for the fiducial mass and velocity and radial magnetic fields. Thermalization increases with increasing asymmetry. We found similar increases for random and toroidal fields.

Hotokezaka et al. 2013). To estimate the effect on thermalization, we compare a spherical model to an oblate one, where both models have $M_{ej} = 5 \times 10^{-3} M_{\odot}$ and $v_{ej} = 0.2c$, radial magnetic fields, and a broken power-law density profile with $(\delta, n) = (1, 10)$. For the oblate geometry, the density is a function of \tilde{v} , where

$$\tilde{v} = v \sqrt{a^{-2/3} \sin^2 \theta + a^{4/3} \cos^2 \theta}$$

is chosen so that isodensity contours are oblate spheroids of aspect ratio a .

Figure 12 compares the $f(t)$ for the oblate and spherical cases, and shows that massive particle thermalization increases with increasing asphericity. For an aspect ratio $a = 4$, the $f(t)$ for α ’s, β ’s, and fission fragments increase by a factor of ~ 1.5 relative to spherical ejecta. γ -ray thermalization is higher for the oblate geometry, but only slightly. The higher $f(t)$ are due to the higher density of the oblate ejecta, which more than compensates for the increased ease of escape in directions perpendicular to the equatorial plane. Figure 12 shows $f(t)$ only for radial magnetic fields, but we found similar increases for random and toroidal fields.

5.2. Total Heating Efficiency

To study the net heating efficiency, we convolve $f(t)$ for each decay product with the fraction that particle contributes to the total energy generation. The bottom panel of Figure 13 shows how the r -process decay energy is divided among different particles, while the top panel shows the energy *thermalized* by each particle type as a fraction of the total energy emitted across all decay channels. The $f(t)$ represented in Figure 13 are for a fiducial ejecta model with moderately tangled ($\lambda = 0.25$) magnetic fields. The total thermalization efficiency, which is simply a sum over particle types, is plotted in black. While γ ’s, α ’s, β ’s, and fission fragments all have $f(t) \approx 1$ at very early times, the initial *total* thermalization efficiency is less than one because a significant fraction of the β -decay energy is lost to neutrinos.

The net thermalization efficiency, in this model, drops below 0.5 by $t = 1$ day, and below 0.1 by $t \sim 10$ days. Though β -particles and γ -rays dominate the energy production at all

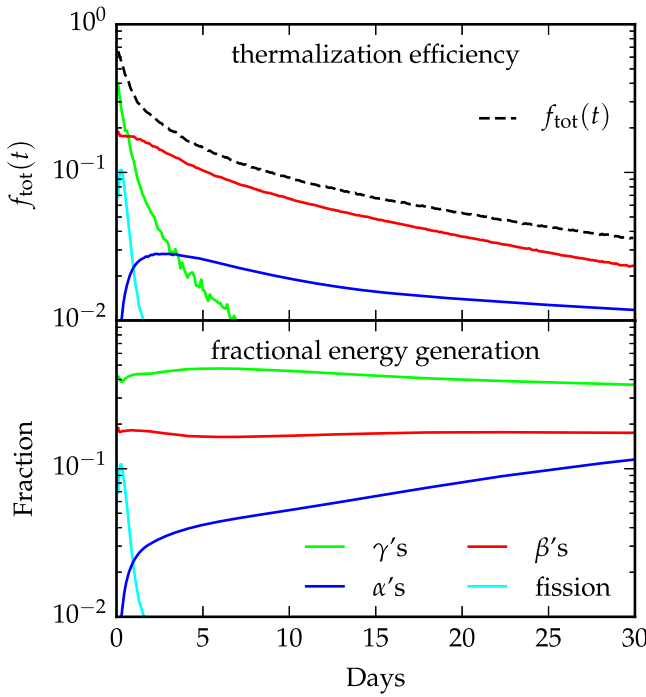


Figure 13. Bottom panel: the fractional energy generation associated with each type of particle, from r -process simulations using the FRDM mass model. The division of β -decay energy among β -particles, γ -rays, and neutrinos was calculated for our representative SPH trajectory with $Y_{e,0} = 0.04$. Top panel: the fractions from the bottom panel, convolved with $f(t)$ for each particle, for the fiducial model with random magnetic fields. The total thermalization efficiency, f_{tot} , plotted as a dashed black line, is the sum of the particle-specific curves. β - and α -particles supply most of the thermalized energy.

times, γ -rays thermalize inefficiently, and supply very little heating after $t \sim 1$ day. While α -decay produces less than $\sim 10\%$ of the total energy, the α -particles thermalize fairly efficiently, and so contribute a significant fraction of the total thermalized energy.

The total heating efficiency has the expected dependence on the ejecta parameters: greater masses and lower velocities lead to higher $f_{\text{tot}}(t)$, as shown in Figure 14. Thermalization for the low-mass and high-velocity models falls below 0.5 within a few days, and below 0.2 by 5–7 days. The high-mass and low-velocity models thermalize much more efficiently, sustaining $f_{\text{tot}}(t) > 0.5$ out to $t \lesssim 1$ week, and not falling below $f_{\text{tot}}(t) = 0.2$ until $t \sim 15$ –20 days. There is also variation within each model (up to a factor of ~ 2) due to uncertainties in the magnetic field.

5.2.1. Dependence on Nuclear Physics

The radioactive energy generation—and therefore the thermalization—depends on r -process yields, which in turn are sensitive to variations in nuclear physics models and astrophysical conditions. To explore this effect, we consider r -process yields computed for different mass models, and for different initial Y_e of the ejected matter.

The yields differ primarily in the amount of translead nuclei synthesized relative to lighter r -process elements. Mendoza-Temis et al. (2015) have shown that the production of translead nuclei is sensitive to nuclear physics inputs, in particular to neutron separation energies near $N = 130$. As discussed in

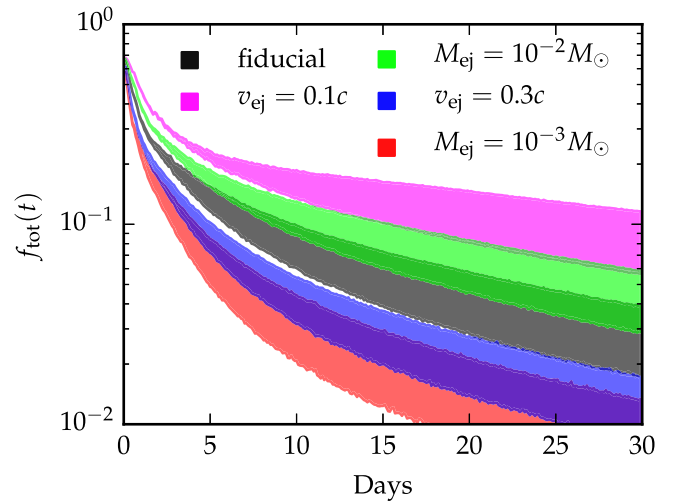


Figure 14. Total thermalization efficiencies for different ejecta models ($M_{\text{ej}}, v_{\text{ej}}$) using FRDM energy-generation rates. The fiducial model is plotted in black. Other curves differ from the fiducial model in M_{ej} or v_{ej} only. The width of the curves reflects the variation in $f(t)$ for different magnetic field configurations; the curves are bounded on top by $f_{\text{tot}}(t)$ for a toroidal field and on bottom by $f_{\text{tot}}(t)$ for a radial field configuration.

Section 2.3, the production of translead nuclei also depends on initial electron fraction, decreasing as $Y_{e,0}$ increases.

R -process yields could impact thermalization in two ways. First, different yields have different abundance-averaged compositional properties, and could give rise to different thermalization rates. Second, because nuclei heavier than lead decay mainly by fission and α -emission, while lighter nuclei undergo β -decay, the amount of translead material will alter the relative importance of α - and β -decay. Since all α -decay energy is transferred to energetic α -particles, which thermalize efficiently, while $\gtrsim 70\%$ of β -decay energy goes to γ -rays and neutrinos, which do not, enhanced α -decay may increase thermalization. Based on these arguments, we expect that differences in the amounts of translead nuclei will result in different $f_{\text{tot}}(t)$, and therefore, differences in predicted kilonova light curves.

To explore the strength of these effects, we compare the thermalization efficiency for three different compositions: the reference r -process yields (based on the FRDM mass model); yields for the DZ31 mass model, which predicts increased production of translead nuclei (see Figure 1); and yields from a calculation using the FRDM model with $Y_{e,0} = 0.25$.

We found that the DZ31 model predicts a composition whose abundance-averaged properties and emission spectra are very similar to those predicted by the FRDM model. We therefore expect that the different yields found for the DZ31 model will not significantly change $f(t)$ for individual particles. In contrast, the high- $Y_{e,0}$ composition has average compositional properties and emission spectra that diverge from the reference case (FRDM, $Y_{e,0} = 0.04$), so we calculate for this composition $f(t)$ of all individual decay products for our fiducial ejecta ($M_{\text{ej}} = 5 \times 10^{-3} M_{\odot}, v_{\text{ej}} = 0.2c$). The thermalization timescales, plotted in Figure 11 as open triangles, are similar to those for the standard low- $Y_{e,0}$ composition. For both the DZ31 and high- $Y_{e,0}$ cases then, impacts on $f_{\text{tot}}(t)$ are the results of differences in the relative importance of each heating channel, not differences in how efficiently individual decay products thermalize.

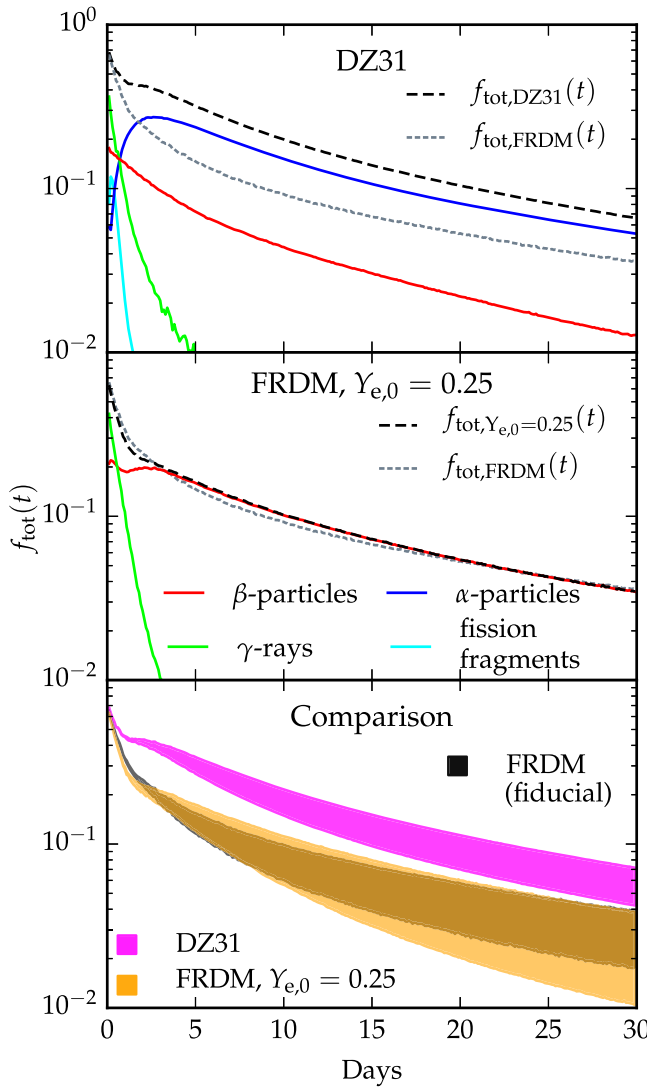


Figure 15. Effect of nuclear physics inputs on total thermalization efficiency. Top and middle panels: $f(t)$ (fiducial M_{ej} , v_{ej} ; random fields) convolved with fractional energy-generation rates for the DZ31 nuclear mass model (top panel) and a high- $Y_{e,0}$ FRDM trajectory (middle panel). Solid lines show the fraction of emitted energy thermalized by each particle as a function of time, and $f_{tot}(t)$ is plotted in black dashed lines. Bottom panel: the range of $f_{tot}(t)$ expected for each of the cases shown in the top two panels. We plot $f_{tot}(t)$ for the low- $Y_{e,0}$ FRDM composition in black for comparison. The widths of the curves are due to the range of possible magnetic field configurations.

Figure 15 compares $f_{tot}(t)$ for the three cases studied. In the top panel, we show $f_{tot}(t)$ and the contributions from each decay product, determined using energy-generation rates from the DZ31 nuclear mass model abundances, for which α -decay dominates the energy production at late times. The middle panel shows an analogous calculation for the FRDM model with $Y_{e,0} = 0.25$, which has negligible late-time α -decay. In the bottom panel, we compare $f_{tot}(t)$ for these models with the fiducial FRDM model. The greater role of α -decay in the DZ31 model increases $f_{tot}(t)$ by a factor of $\gtrsim 1.5$, mainly due to the fact that less energy is lost in neutrinos and γ -rays, which thermalize very inefficiently. In the fiducial composition α -decay and fission produce only a small fraction of the energy, so the effect of increasing $Y_{e,0}$ is modest. A stronger effect might be seen for DZ31, which produces more translead nuclei when $Y_{e,0}$ is low, and is therefore more likely to experience dramatic decreases in translead production when the initial electron fraction rises.

6. EFFECT ON KILONOVA LIGHT CURVES

To determine the effect of thermalization on kilonova observables, we incorporated our results for $f_{tot}(t)$ into the time-dependent Monte Carlo radiation transport code Sedona (Kasen et al. 2006), and carried out light curve calculations. The calculations here resemble those of Barnes & Kasen (2013), but include thermalization effects.

6.1. Analytic Fit to Thermalization Efficiency

For easy inclusion of thermalization in light curve simulations, we propose a simple analytic formula for $f_{tot}(t)$, which provides a good fit to our detailed numerical calculations,

$$f_{tot}(t) = 0.36 \left[\exp(-at) + \frac{\ln(1 + 2bt^d)}{2bt^d} \right], \quad (34)$$

where a , b , and d are fitting constants. The parameterized form of Equation (34) is motivated by our approximate analytic solutions for $f(t)$ (Equations (32) and (33)), with slight modifications to improve the quality of the fit and account for energy lost to neutrinos. Table 1 gives the best-fit parameters for all the ejecta models considered for energy-generation rates of the FRDM nuclear mass model. A comparison of Equation (34) to numerical results is presented in Figure 16. For simplicity, Figure 16 shows results only for random magnetic fields. However, our model provides an equally good fit for radial and toroidal fields.

We found that, in the case of the FRDM mass model, compositions from high- $Y_{e,0}$ ejecta have thermalization profiles similar to compositions from initially neutron-rich ejecta. This suggests that our thermalization models may be appropriate for material ejected dynamically and from disk winds, regardless of the initial electron fraction. However, we note that the insensitivity of $f_{tot}(t)$ to $Y_{e,0}$ may not be as robust for other nuclear mass models. The effect of $Y_{e,0}$ may be particularly pronounced for the DZ31 model, which produces large amounts of translead nuclei, and therefore predicts significant α -decay. Changes in $Y_{e,0}$ could inhibit the production of these nuclei, decrease the role of α -decay, and thus alter thermalization efficiency. The effect on $f_{tot}(t)$ would be much stronger than for the FRDM model, which does not produce many translead nuclei even for favorable $Y_{e,0}$.

6.2. Light Curves

The net thermalization efficiency, $f_{tot}(t)$, has a significant impact on kilonova luminosity. Figure 17 compares bolometric light curves calculated using our derived $f_{tot}(t)$ to those assuming 100% thermalization. We also show results for a treatment which propagates γ -rays, but assumes charged particle energy thermalizes instantly. This was the method used to estimate $f_{tot}(t)$ in earlier Sedona kilonova simulations, including Barnes & Kasen (2013).⁵ (A similar simplification was invoked in the discussion of net heating by Hotokezaka et al. 2016.) For all radiation transport simulations,

⁵ Sedona's original treatment of thermalization assumed that β -decay generated 90% of the r -process decay energy, with fission accounting for the other 10%. Of the β -decay energy, 25% was taken to be lost to neutrinos, and the remaining 75% was split evenly between β -particles and γ -rays. The energy from β -particles and fission fragments was thermalized promptly, while the energy from γ -rays was converted into 1 MeV photons, which were propagated through the ejecta in a Monte Carlo transport scheme.

Table 1
Analytic Fit Parameters for $f_{\text{tot}}(t)$

Model M/M_{\odot}	v_{ej}/c	Coefficients								
		Random			Radial			Toroidal		
		a	b	d	a	b	d	a	b	d
1×10^{-3}	0.1	2.01	0.28	1.12	2.17	0.26	1.51	2.04	0.26	1.07
1×10^{-3}	0.2	4.52	0.62	1.39	4.75	0.76	1.68	4.63	0.55	1.39
1×10^{-3}	0.3	8.16	1.19	1.52	8.57	1.58	1.77	8.36	1.08	1.53
5×10^{-3}	0.1	0.81	0.19	0.86	0.91	0.12	1.28	0.81	0.19	0.79
5×10^{-3}	0.2	1.90	0.28	1.21	2.04	0.26	1.53	1.94	0.26	1.20
5×10^{-3}	0.3	3.20	0.45	1.39	3.36	0.48	1.63	3.26	0.41	1.39
1×10^{-2}	0.1	0.56	0.17	0.74	0.62	0.10	1.16	0.55	0.18	0.65
1×10^{-2}	0.2	1.31	0.21	1.13	1.43	0.17	1.46	1.34	0.19	1.11
1×10^{-2}	0.3	2.19	0.31	1.32	2.32	0.30	1.57	2.24	0.28	1.32
5×10^{-2}	0.1	0.27	0.10	0.60	0.26	0.07	0.85	0.27	0.10	0.54
5×10^{-2}	0.2	0.55	0.13	0.90	0.61	0.08	1.24	0.56	0.13	0.85
5×10^{-2}	0.3	0.95	0.15	1.13	1.01	0.12	1.39	0.96	0.14	1.11

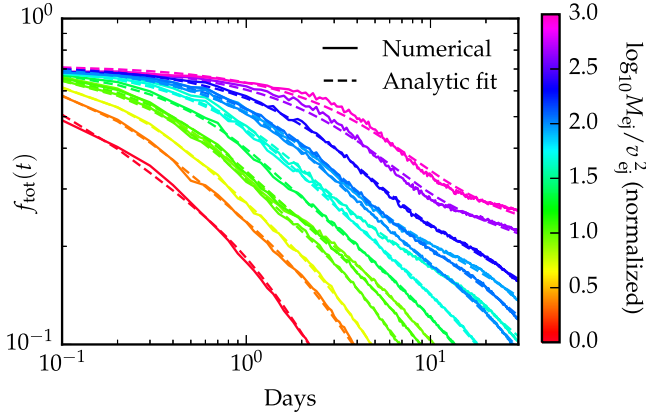


Figure 16. Numerical results for $f_{\text{tot}}(t)$ (solid lines) compared to the analytic fit (dashed lines) given by Equation (34) for random magnetic fields and all (M_{ej} , v_{ej}) considered. The lines are color-coded by the base-10 logarithm of the ratio $M_{\text{ej}}/v_{\text{ej}}^2$, which we have normalized to the minimum value found in our suite of models. Equation (34) fits results from radial and toroidal fields with similar success.

we have used the simplified composition and the boosted, synthetic r -process opacities of Kasen et al. (2013). We consider here only models with low $Y_{e,0}$, which robustly produce r -process elements including Lanthanides and Actinides, making our choice of opacity appropriate. Models with higher initial electron fractions may fail to produce these heavy elements. The opacities for such models would be much lower, and the associated light curves would be shorter, brighter, and bluer (e.g., Metzger et al. 2010; Barnes & Kasen 2013; Kasen et al. 2015).

Figure 17 shows that our more accurate treatment of thermalization impacts predicted photometry for all ejecta models considered. Relative to earlier calculations with less sophisticated thermalization schemes, we find kilonova light curves peak slightly earlier, have lower luminosities at peak, and have much dimmer late-time luminosities. The effects of thermalization are most pronounced for less massive and higher velocity ejecta models, which are dimmer and fade more quickly than their slower, more massive counterparts.

The uncertainties complicating the calculation of $f_{\text{tot}}(t)$, outlined in earlier sections, lead to uncertainties in light curve calculations. The most important of these are illustrated in the

middle panel of Figure 17, which presents bolometric light curves for our fiducial ejecta model for all magnetic fields considered and for the DZ31 nuclear mass model. The effect of field configuration is straightforward; random or toroidal fields trap particles, enhance $f_{\text{tot}}(t)$, and produce more luminous kilonovae relative to radial fields. The nuclear mass model plays a role by determining the yields of translead nuclei, and therefore the amount of energy produced by α -decay. Models, like DZ31, that derive a sizable fraction of their radioactive energy from α -decay, have a higher $f_{\text{tot}}(t)$, and therefore greater bolometric luminosity. The luminosity increase for the DZ31 composition is a result both of higher $f_{\text{tot}}(t)$ due to more α -decay, and to the greater absolute amount of energy produced by r -process decay for the DZ31 model relative to the FRDM model (see Section 2.4.) Ejecta geometry, which we have not explored in Figure 17, can also affect observed light curves, by altering $f_{\text{tot}}(t)$ (see Section 5.1.1) and by introducing viewing angle dependence. 3D kilonova simulations are needed to fully explore and document these uncertainties.

Though thermalization can impact kilonovae’s bolometric luminosities substantially, it has little effect on their characteristic red colors, which are derived from a composition rich in Lanthanides. Figure 18 shows the broadband evolution of our fiducial ejecta for two treatments of thermalization, one which includes time-dependent $f_{\text{tot}}(t)$, and one which relies on the simple γ -ray transport scheme of Barnes & Kasen (2013). Including $f_{\text{tot}}(t)$ leads to dimmer light curves in all bands (a result of the kilonova’s lower energy budget), but does not change the relative strengths of the broadband curves. The effect of thermalization on a kilonova’s spectral energy distribution is therefore minor.

6.3. Implications for the Kilonova Accompanying GRB 130603B

An excess near-infrared (NIR) flux discovered in the afterglow of the short γ -ray burst GRB 130603B has been widely interpreted as a kilonova (Berger et al. 2013; Tanvir et al. 2013). Tanvir et al. (2013) determined that the source of the flux had an absolute AB magnitude in the J -band of -15.35 at $t \sim 7$ days. Having incorporated $f_{\text{tot}}(t)$ into kilonova light curve models, we can more confidently constrain the mass ejected in the kilonova associated with GRB 130603B.

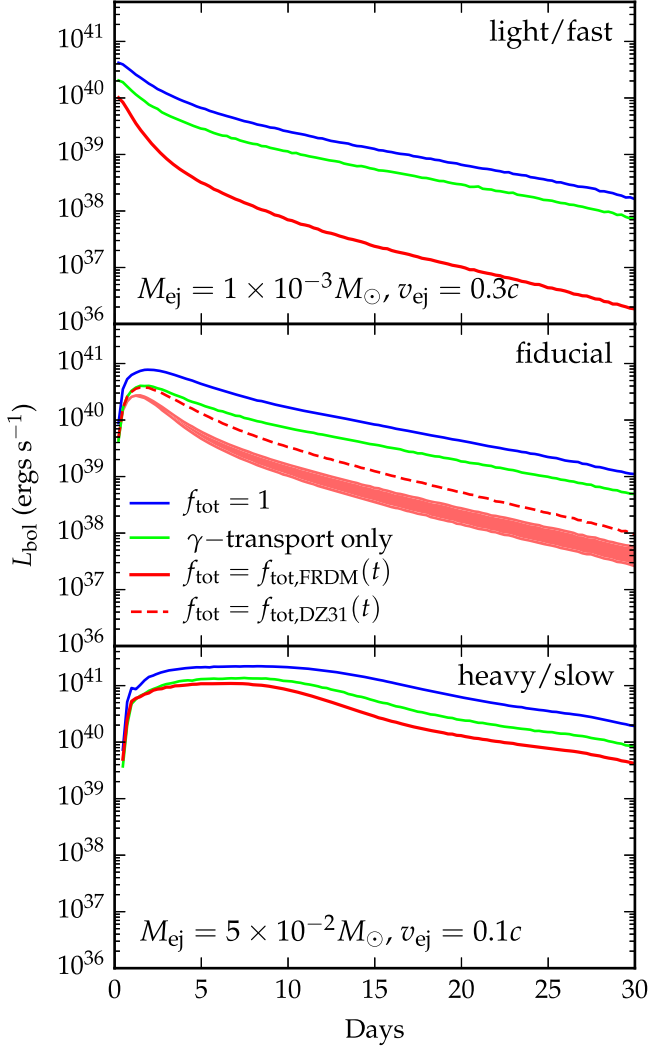


Figure 17. Synthetic bolometric light curves calculated with Sedona for three different treatments of thermalization: full thermalization (blue curves); Sedona’s original thermalization scheme, which deposits charged particle energy but explicitly tracks the deposition of γ -ray energy (lime curves); and the time-dependent $f_{\text{tot}}(t)$ from our numerical simulations (red curves). Light curves in the top and bottom panels adopt $f_{\text{tot}}(t)$ given by random fields and the FRDM mass model. To illustrate the effect of uncertainties in $f_{\text{tot}}(t)$ on light curves, we plot for our fiducial model (middle panel) L_{bol} for a range of magnetic fields (thick red curve) and for the DZ31 mass model (red dashed curve). Accounting for time-dependent thermalization efficiencies has a significant impact on kilonova luminosity, particularly for models with lower masses and higher velocities. For our fiducial model, the predicted luminosity is lower by a factor of $\lesssim 2$ at peak, and by 10 days is lower by an factor of 5.

In Figure 19, we compare the detected flux to J -band light curves for various ejecta models, and find the observed flux is consistent with $5 \times 10^{-2} M_{\odot} \lesssim M_{\text{ej}} \lesssim 10^{-1} M_{\odot}$. This mass is higher than what is typically predicted for the dynamical ejecta from a binary NS merger, suggesting that if the kilonova interpretation is correct, the progenitor of GRB 130603B was perhaps an NSBH merger, or that the mass ejected was significantly enhanced by post-merger disk winds.

Our mass estimate here is an improvement over earlier work which neglected detailed thermalization, and gives substantially different results. For example, Piran et al. (2014) suggested $M_{\text{ej}} \sim 0.02 M_{\odot}$, less than half our new value. However, we have not accounted for viewing angle effects.

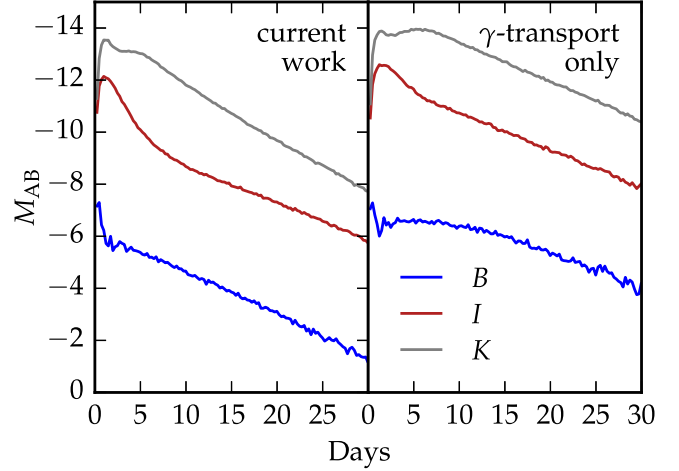


Figure 18. Select broadband light curves for our fiducial ejecta model for two treatments of thermalization: full $f_{\text{tot}}(t)$ (left panel), and the cruder treatment employed in earlier kilonova calculations (right panel). The curves are dimmer in the newer models, reflecting the reduction in thermalized energy, but relationships between the light curves in the various bands is mostly unchanged, so the kilonova colors are preserved.

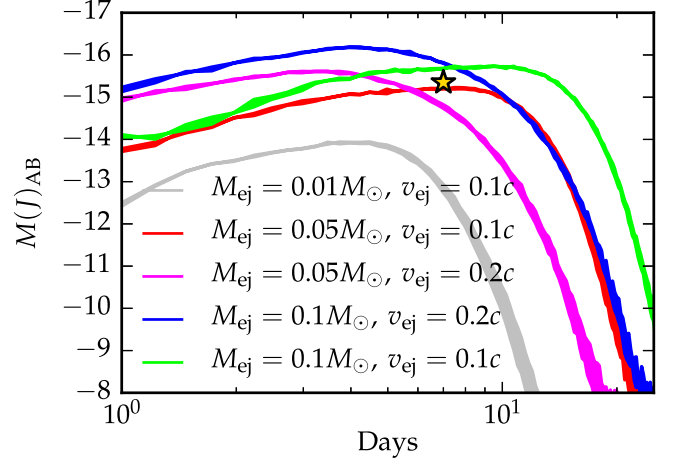


Figure 19. Absolute (AB) J -band light curves for several ejecta models. As in earlier figures, the width of the curves is produced by differences in $f_{\text{tot}}(t)$ due to different magnetic field configurations. The excess IR flux (gold star) suggests an ejected mass between 5×10^{-2} and $10^{-1} M_{\odot}$.

If the ejected material is mainly confined to the equatorial plane, the emission will be brighter when the system is viewed face-on (Roberts et al. 2011), which would reduce the inferred mass somewhat. In an oblate ejecta, thermalization will also be more efficient, which could have a small impact on mass measurements. Finally, we note that different nuclear mass models predict different rates of radioactive heating and differing $f_{\text{tot}}(t)$, which introduces additional uncertainties into our mass estimate. Radiation transport simulations in three dimensions with time-dependent thermalization models will better constrain M_{ej} .

6.4. Late-time Light Curve

Late-time kilonova light curves may probe the history of r -process nucleosynthesis in CO mergers. At ~ 2 days after merger, fission ceases to be important, and α - and β -decay dominate the kilonova’s energy supply. Energy from α -decay is transferred entirely to fast α -particles, which thermalize

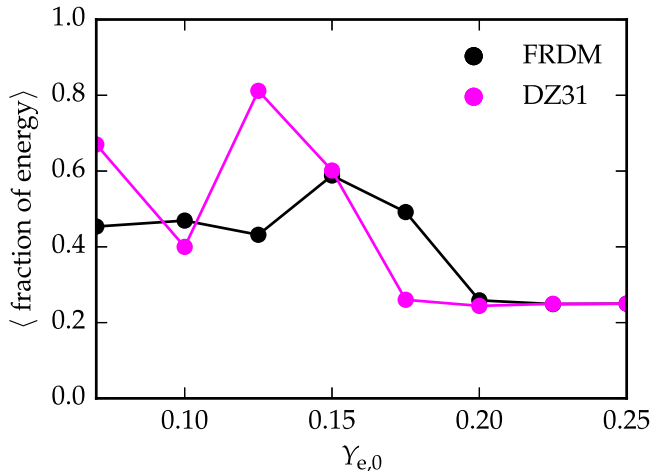


Figure 20. Time-averaged fraction of the r -process decay energy emitted as β - and α -particles and fission fragments, as a function of initial Y_e . The data was taken from r -process calculations on our representative SPH trajectory, with $Y_{e,0}$ artificially altered. The lower the initial electron fraction is, the more energy from α -decays is available to drive a late-time light curve.

fairly efficiently out to late times. β -particles thermalize with similar efficiency, but carry only a fraction ($\sim 25\%$) of the total β -decay energy, with the rest lost to neutrinos and γ -rays. A kilonova's late-time luminosity will therefore depend on the relative importance of α - versus β -decay. Because only nuclei with $200 \lesssim A \lesssim 250$ undergo α -decay, the late-time kilonova luminosity may diagnose the presence of heavy elements in the ejecta, and therefore constrain the neutron-rich conditions required for heavy element formation.

We gauge the relative strength of late-time kilonova light curves for different $Y_{e,0}$ by estimating the percent of energy from the decay of r -process elements emitted as fission fragments, α -, and β -particles, time-averaged over $t = 10$ –100 days. (Note that while all energy from α -decay emerges as α -particles, β -particles receive only 25%–30% of the energy from β -decay.) The results for our representative SPH trajectory, for a range of $Y_{e,0}$ and two nuclear mass models, are shown in Figure 20. The curves suggest that systems with $Y_{e,0} \lesssim 0.17$ have more robust late-time heating, and are likely to exhibit late-time light curves that are more luminous by a factor of up to ~ 2 .

If fission is more significant at late times than our calculation predicts (e.g., Hotokezaka et al. 2016 find that fission supplies $\gtrsim 10\%$ of the total energy out to late times), the dependence of the late-time light curve on $Y_{e,0}$ could be much stronger. Fission fragments thermalize extremely well past maximum light. Since very neutron-rich conditions are needed to build up the heavy nuclei ($A \gtrsim 250$) that undergo fission, in a strongly fissioning ejecta, late-time luminosity could depend sensitively on $Y_{e,0}$.

A key observable for probing the nuclear physics of CO mergers may be the ratio of the kilonova luminosity measured at peak brightness to that observed on the light curve tail. At peak, the luminosity is found to roughly equal the instantaneous energy deposition rate (“Arnett’s Law,” Arnett 1982). At $t \gg t_{\text{peak}}$, when the ejecta becomes transparent, the emergent luminosity again tracks the energy deposition rate. Assuming the radioactive energy released by r -process material follows a power law, $\dot{\epsilon} \propto t^{-\eta}$, the ratio of peak luminosity to luminosity

at some later time, $t_{\text{tail}} > t_{\text{peak}}$, is

$$\frac{L(t_{\text{peak}})}{L(t_{\text{tail}})} = \left(\frac{t_{\text{peak}}}{t_{\text{tail}}} \right)^{-\eta} \frac{f_{\text{tot}}(t_{\text{peak}})}{f_{\text{tot}}(t_{\text{tail}})}. \quad (35)$$

If the decay index, η , is reasonably constrained, measuring this luminosity ratio provides some handle on the thermalization efficiency $f_{\text{tot}}(t)$ and hence the presence of α -decaying or fissioning translead isotopes, which enhance $f_{\text{tot}}(t)$ at late times. In general, this ratio will depend on M_{ej} , v_{ej} , and magnetic field configuration, as well as translead abundance. However, M_{ej} and v_{ej} can be constrained by other light curve properties, including rise time and peak brightness. In cases where these degeneracies can be untangled, the luminosity ratio may be a useful diagnostic of translead production.

As a simple test case, we consider light curves for our fiducial ejecta model calculated for the FRDM (low α -decay) and DZ31 (high α -decay) mass models. Setting $t_{\text{tail}}/t_{\text{peak}} = 5$, we find that $L_{\text{peak}}/L_{\text{tail}}$ is higher for the FRDM case by $\sim 10\%$, an effect due entirely to differences in translead production. While differences of this magnitude may be difficult to identify given other uncertainties, the effect of translead isotopes’ decay will be stronger at later times, and for systems with high rates of late-time fission. If, as considered earlier, fission contributes 10% of the radioactive energy at late times, the peak-tail luminosity ratio will be enhanced by a factor of ~ 2 relative to our reference case, which has negligible late-time fission.

More detailed studies are needed to fully explore and clarify the relationship between light curves and composition, and we defer such an exploration to later work. Even if extracting constraints on the nuclear physics proves challenging, the luminosity ratio could provide information about $f_{\text{tot}}(t)$, which would aid in understanding the ejecta’s mass, energy, and magnetic fields.

7. CONCLUSION

We have shown that the radioactive energy from the decay of r -process material does not completely thermalize in the ejecta from CO mergers. For the first time, we have explicitly simulated the thermalization of all suprathermal r -process decay products in the heavy-element-rich kilonova ejecta. From these simulations, we derived time-dependent expressions for the net kilonova thermalization efficiency, $f_{\text{tot}}(t)$, for models spanning a range of expected ejecta masses and velocities. For most parameters studied, $f_{\text{tot}}(t)$ drops below 0.5 within 5 days after the merger. At 15 days after merger, $f_{\text{tot}}(t)$ may be as low as 0.01–0.1. Thermalization therefore has a significant impact on the peak luminosity of kilonovae and the late-time light curve decline rate.

We have also explored the dependence of $f_{\text{tot}}(t)$ on electron fraction and nuclear mass model, and outlined how variations in these parameters may systematically affect thermalization. In general, systems that favor the production of translead nuclei have higher thermalization efficiencies at late times. This is because a greater fraction of radioactive energy is emitted through α -decay and fission channels, which thermalize more efficiently than energy from β -decays, since less energy is lost to γ -rays and neutrinos.

We have presented updated radiation transport simulations that incorporate our new calculations of time-dependent thermalization, and find that thermalization has a significant effect on the predicted photometry of kilonovae. Compared to older models that neglected detailed thermalization, our new

light curves peak earlier and at lower luminosities, and are much dimmer (by a factor of ~ 10) at late times ($\gtrsim 15$ days after peak). Our new models of kilonova with Lanthanide-rich r -process ejecta keep their characteristic red color, and are much more luminous in infrared (I -, J -, and K -) bands than in the optical.

Our results have consequences for detecting kilonovae, whether blindly or as counterparts to GW events. While our new models retain the red color believed to be a defining kilonova signature, the rapid decline of $f_{\text{tot}}(t)$ poses a challenge to detection, and underscores the necessity of timely follow-up of GW triggers. Since $f_{\text{tot}}(t)$ is lower and declines more quickly in less massive systems, this is especially important for kilonovae generated by merging NSs, which are typically expected to be less massive than BHNS kilonovae by a factor of ~ 10 .

The recent detection of the GW event GW150914 (Abbott et al. 2016b) spurred a slew of EM follow-up activities (Abbott et al. 2016a; Soares-Santos et al. 2016). While the GW signal turned out to be the result of a binary BH merger, which is not expected to have an EM counterpart, the follow-up campaign offers a sense of the prospects of detecting a kilonova counterpart to future GW events. From a kilonova standpoint, some of the most promising observational efforts were carried out by the Dark Energy Camera (DECam), which had limiting (AB) magnitudes $i < 22.5$ and $z < 21.5$; the VLT Survey Telescope (VLS), which reached $r < 22.4$, and VISTA, with $J < 20.7$.

Had the GW trigger been due to a typical NSBH merger located 100 Mpc distant, the associated kilonova ($M_{\text{ej}} = 5 \times 10^{-2} M_{\odot}$; $v_{\text{ej}} = 0.2c$) could have been observed by DECam in i and z for $t \lesssim 7$ days; by VST in r for $t \lesssim 5$ days; and by VISTA in J for $t \lesssim 8$ days. The situation is less promising for a NS² merger ejecting less mass ($M_{\text{ej}} = 5 \times 10^{-3} M_{\odot}$; $v_{\text{ej}} = 0.2c$), which will be intrinsically dimmer and suffer from less efficient thermalization. To be visible to DECam in i (z) at peak, such a system would need to be closer than ~ 63 (~ 57) Mpc, while VISTA (VST) could only detect it at distances less than ~ 52 (~ 10) Mpc.

This analysis highlights the importance of seeking optical counterparts at early times, before they fade below detection thresholds. It also suggests that observing strategies should focus on depth, rather than area, to improve the chances of detecting signals that are likely to be faint. Lastly, these findings emphasize the criticality of developing facilities with greater IR sensitivity. *Euclid* (Amendola et al. 2012) and *WFIRST* (Green et al. 2012), each which will have an H -band depth of ~ 25 , could detect a typical NS² kilonova, located at 100 Mpc, out to $t \sim 15$ days.

Our calculation of time-dependent thermalization efficiencies for kilonovae constrains a key uncertainty in models of r -process transients. Additional work can further improve these models. We have focused on thermalization in the dynamical ejecta from CO mergers, but the ideas developed here could—and should—be applied to study disk wind outflows, which may produce ejecta poor in Lanthanides and Actinides and potentially contribute a blue/optical component to kilonova light curves. Calculating heating efficiencies for the multiple components believed to make up a kilonova, and incorporating realistic models of $f_{\text{tot}}(t)$ in 3D radiation transport simulations of multi-component light curves would yield the best predictions to date of kilonovae’s EM signatures.

This work is supported in part by a Department of Energy Office of Nuclear Physics Early Career Award, and by the Director, Office of Energy Research, Office of High Energy and Nuclear Physics, Divisions of Nuclear Physics, of the U.S. Department of Energy under Contract No. DE-AC02-05CH11231, and from NSF grant AST-1206097. Support for M.-R.W. and G.M.-P. is provided in part by the Helmholtz Association through the Nuclear Astrophysics Virtual Institute (VH-VI-417) and the BMBF-Verbundforschungsprojekt number 05P15RDFN1.

APPENDIX TRANSPORT METHODS

This appendix describes our numerical method for calculating detailed thermalization efficiencies using a 3D particle transport scheme.

A.1. Grid

We carry out our calculation on a 3D Cartesian grid of 100^3 zones. The ejecta is assumed to have a broken power-law density profile and a two-zone composition, as described in Section 2. The grid is initialized at $t = 0.1$ days, and advanced in time every 0.1 days.

In each time step, the grid emits N_{pack} particle packets with cmf kinetic energy E_{pack} equal to $E_{\Delta t}(t)/N_{\text{pack}}$, where $E_{\Delta t} = M_{\text{ej}} \int_{\Delta t} \dot{\epsilon}(t) dt$ is the total radioactive energy emitted by the ejecta over the course of the time step. The probability of emission in any zone is proportional to zone mass. Packets are emitted at random positions within the zone, with random initial directions, at a time selected from a flat distribution $[t, t + \Delta t]$. Each packet represents N_{part} particles of energy E_{part} , where the particle’s initial cmf energy is sampled from the time-dependent spectra of Figure 3. Particles are transported through the grid until their cmf energy falls below a threshold energy ~ 1000 times less than the typical energy at emission. At this point, particles deposit their residual kinetic energy and are removed from the grid.

A.2. γ -rays

γ -ray packets are propagated through the grid in small steps in typical Monte Carlo fashion (e.g., Lucy 2005; Kasen et al. 2006.) A propagating photon packet can reach the end of the current grid time step, leave the zone it is in, or interact with an atom. The outcome that occurs on the shortest timescale is selected. The timescales for the first two processes are straightforward, and the timescale for interaction is given by

$$\Delta t_{\text{atom}} = -\frac{1}{c\rho\kappa_{\text{tot}}} \ln(1-z), \quad (36)$$

where $\kappa_{\text{tot}} = \kappa_{\text{C}} + \kappa_{\text{PI}}$ is the sum of Compton and photoionization opacities, ρ is the mass density, and z is a random number sampled from $(0, 1)$. The relative weights of κ_{C} and κ_{PI} determine whether the γ -ray packet Compton scatters or photoionizes.

During a Compton scatter, a photon undergoes some angular displacement, with the differential cross section and change in energy given by the Klein–Nishina formula. Energy lost by the photon packet is transferred to a non-thermal electron, which also acquires a momentum opposite to that of the post-scatter

photon. The electron is then transported through the grid, as described in the next section.

In a photoionization, some of the photon's energy thermalizes promptly, but the rest is transferred to a non-thermal photoelectron. In general, photoelectrons are ejected from the inner shells of the ionized atoms, and acquire energies equal to the γ -ray energy less the photoelectron's binding energy, E_B . Outer shell atomic electrons cascade down to fill the vacancy created by the ionization, releasing photons whose energies sum to $\sum E = E_B - \Delta E_{\text{atom}}$, where ΔE_{atom} is the difference in the atom's total energy before and after the ionization and cascade. The ejected photoelectron will travel through the grid until it thermalizes and recombines with an ambient atom. Since the thermalized electron will attach to the atom's valence shell, the energy released upon recombination will be low, on the order of ΔE_{atom} .

We assume that all photoelectrons originate from inner shells of heavy elements, so $E_B \gg \Delta E_{\text{atom}}$. The energy released in the post-ionization cascade is then $E_B - E_{\text{atom}} \approx E_B$. This energy thermalizes immediately. The photoelectron receives the remainder of the γ -ray energy, $E_\gamma - E_B$, and a momentum parallel to the initial γ -ray momentum. It is propagated until it dissipates its kinetic energy.

Since the cross section for photoionization peaks at $E_\gamma \sim E_B$, we estimate representative binding energies for the r -process composition by locating local maxima in the aggregate photoionization opacity curve. For each photoionization, we select the minimum binding energy such that $E_\gamma^{\text{cmf}} > E_B$. If $E_\gamma^{\text{cmf}} \gtrsim 0.1$ MeV, and there are no identifiable peaks that satisfy this criterion, we set $E_B = 0.9E_\gamma^{\text{cmf}}$.

A.3. Massive Particles

Massive particles lose energy continuously, so are not suited to a discrete Monte Carlo treatment. Instead, a massive particle packet is transported through the grid until it reaches the border of its zone, the grid time step ends, or (in the case of disordered fields) the magnetic field changes direction. The change in the particle's cmf energy is calculated from the particle's initial cmf energy, and the zone conditions and elapsed time, both measured in the cmf. The particle energy is then adjusted.

For α -particles and fission fragments, all energy lost is assumed to be thermalized and promptly deposited on the grid. In the case of β -particles, energy loss via Bremsstrahlung can be significant, and a non-negligible fraction of the β -particle energy can be converted to photons of fairly high energies, which will not immediately thermalize. To account for this possibility, we differentiate β -particle energy lost to plasma and ionization/excitation—which we assume thermalizes instantly—from energy lost to Bremsstrahlung, which we assume does not. At the end of each time step, thermalized energy ΔE_{th} is deposited in the grid, and E_{part} and E_{pack} are adjusted accordingly. The probability that the β -packet is converted to a γ -packet is given by the ratio of the energy lost to Bremsstrahlung during the preceding time step to the particle energy after thermalization: $P_{\beta \rightarrow \gamma} = \Delta E_{\text{Br}} / (E_{\beta,i}^{\text{cmf}} - \Delta E_{\text{th}})$, and random number sampling determines the outcome. If the packet remains a β -packet, E_{part} is decremented by ΔE_{Br} , while E_{pack} remains the same (i.e., N_{pack} is updated.) If conversion to a γ -packet is selected, a new direction of propagation is set randomly in the co-moving frame. The cmf energy of the new γ -ray is selected from a flat probability distribution in the range

(0, $E_{\beta,i}^{\text{cmf}} - \Delta E_{\text{th}}$], which approximates the fairly flat Bremsstrahlung spectrum of relativistic β -particles (Jackson 1999). The value of N_{pack} is then adjusted to preserve total post-thermalization packet energy.

A.3.1. Influence of Magnetic Fields

Charged particles have Larmor radii much smaller than the coherence length of the magnetic field, so we track their motion along field lines without resolving oscillations about the guiding center. The motion of a particle with mass m and kinetic energy E can then be described by the average velocity

$$\langle \mathbf{u} \rangle = v(E)\mu \hat{\mathbf{B}}, \quad (37)$$

where v is the total velocity of a particle with kinetic energy E , $\hat{\mathbf{B}}$ is the unit vector directed along \mathbf{B} , and μ is the cosine of the angle (the “pitch angle”) between the particle's total velocity and the velocity of its guiding center, which is aligned with \mathbf{B} . This $\langle \mathbf{u} \rangle$ is the particle velocity we use to boost between the co-moving and center-of-explosion frames, and to update particle position at the end of a time step.

We explore three classes of magnetic fields: radial ($\mathbf{B} \propto \hat{\mathbf{r}}$), toroidal ($\mathbf{B} \propto \hat{\phi}$), and random. For radial and toroidal fields, the magnetic field direction at any location in the ejecta can be determined trivially, and updating the direction of $\langle \mathbf{u} \rangle$ at the end of each time step is straightforward.

For tangled fields, we randomly choose a unique $\hat{\mathbf{B}}$ for each particle upon emission. We assume the field changes on a length scale $\lambda R_{\text{ej}}(t)$, where λ is a model parameter, and at the beginning of each time step we calculate the timescale for the particle to experience a significant change in $\hat{\mathbf{B}}$:

$$\Delta t_{\text{B}} = \frac{\lambda R_{\text{ej}}(t)}{|\langle \mathbf{u} \rangle|} \ln(1 - z), \quad (38)$$

where z is a random number between 0 and 1. If Δt_{B} is less than the time for a particle to leave a zone or end the grid time step, the magnetic “scattering” action is selected, the particle position and energy are updated, and a new field direction is chosen at random. The re-orientation preserves energy and the magnitude of the momentum in the cmf. This is reasonable because these discrete scatters are standing in for smoother and more gradual field gradients. However, it also leads, on average, to energy losses in the center-of-explosion frame, which decrease thermalization efficiency. This can be thought of as the particles transferring their energy to the bulk kinetic energy of the ejecta rather than the thermal background. It is a small effect.

The propagation of a particle along field lines depends on total velocity and μ . Particles are emitted on the grid with a random direction defined by the unit vector $\hat{\mathbf{D}}$, so μ is $\hat{\mathbf{D}} \cdot \hat{\mathbf{B}}$. In the case of radial fields, μ evolves to preserve the magnetic adiabatic invariant $(1 - \mu^2)/B$. This evolution encourages outward motion. Inward-moving particles encounter ever-stronger fields, and decrease their inward velocity in response, eventually “mirroring” off the field and beginning to travel outward. Particles streaming outward move into weaker magnetic fields, so their pitch angle increases and they stream out even faster.

We include magnetic beaming and mirroring only for radial fields, where changes to the pitch angle facilitate particle

escape and can be meaningful for thermalization. Particles in toroidal fields are confined to one region of velocity space; changes in their pitch angle cannot promote outward motion and so cannot affect thermalization. While particles in random fields could experience beaming and mirroring, they may also undergo pitch angle scattering—interactions with small fluctuations in the field that can change pitch angle, and would act to isotropize μ , counter to beaming and mirroring. We assume the two effects balance out, and hold pitch angle constant for particles in random and toroidal fields.

A.3.2. Fission Fragment Transport

As discussed in Section 2.2, at late times, fission fragments may have Larmor radii comparable to the magnetic field coherence length. This could affect the transport, especially for disordered fields, where field lines in close proximity may have very different orientations. In such a system, the guiding center approximation breaks down, and the motion of the particle must be resolved. We estimate the importance of this effect by modeling fission fragment transport in a tangled field as a random walk of the fragment itself (as opposed to its guiding center). In this simple scheme, fission fragments travel in straight lines and re-orient randomly on length scales of $r_L = r_{L,\max}^{\text{ff}} = 1.0 \times 10^{-2} v_2 t_d R_{\text{ej}}$. This path stands in for the more complicated looping trajectory we would see when $r_L \sim \lambda R_{\text{ej}}$. We carried out a simulation of fission fragment transport in this limit for the fiducial ejecta model, and found only negligible variation in $f_{\text{ff}}(t)$ relative to the flux tube approximation. The difference was apparent only at late times, when fission contributes little to the energy generation. We therefore conclude that detailed models of fission fragment transport are unnecessary.

REFERENCES

- Abadie, J., Abbott, B. P., Abbott, R., et al. 2010, *PhRvD*, **82**, 102001
 Abbott, B. P., Abbott, R., Abbott, T. D., et al. 2016a, arXiv:1602.08492
 Abbott, B. P., Abbott, R., Abbott, T. D., et al. 2016b, *PhRvL*, **116**, 061102
 Amendola, L., Appleby, S., Bacon, D., et al. 2012, arXiv:1206.1225
 Arnett, W. D. 1982, *ApJ*, **253**, 785
 Arnould, M., Goriely, S., & Takahashi, K. 2007, *PhR*, **450**, 97
 Audi, G., Wang, M., Wapstra, A., et al. 2012, *ChPhC*, **36**, 1287
 Barnes, J., & Kasen, D. 2013, *ApJ*, **775**, 18
 Bauswein, A., Goriely, S., & Janka, H.-T. 2013, *ApJ*, **773**, 78
 Bauswein, A., Stergioulas, N., & Janka, H.-T. 2015, arXiv:1503.08769
 Berger, E., Fong, W., & Chornock, R. 2013, *ApJL*, **774**, L23
 Berger, M., Coursey, J., Zucker, M., & Chang, J. 2005, ESTAR, PSTAR, and ASTAR: Computer Programs for Calculating Stopping-Power and Range Tables for Electrons, Protons, and Helium Ions (version 1.2.3) (Gaithersburg, MD: National Institute of Standards and Technology), <http://physics.nist.gov/Star>
 Berger, M., Hubbell, J., Seltzer, S., et al. 2010, XCOM: Photon Cross Section Database (version 1.5) (Gaithersburg, MD: National Institute of Standards and Technology), <http://physics.nist.gov/xcom>
 Berger, M. J., & Seltzer, S. M. 1964, NASSP, **3012**
 Blumenthal, G. R., & Gould, R. J. 1970, *RvMP*, **42**, 237
 Chan, K.-W., & Lingenfelter, R. E. 1993, *ApJ*, **405**, 614
 Dalal, N., Holz, D. E., Hughes, S. A., & Jain, B. 2006, *PhRvD*, **74**, 063006
 Duflo, J., & Zuker, A. P. 1995, *PhRvC*, **52**, R23
 Eichler, D., Livio, M., Piran, T., & Schramm, D. N. 1989, *Natur*, **340**, 126
 Fernández, R., Kasen, D., Metzger, B. D., & Quataert, E. 2015, *MNRAS*, **446**, 750
 Fernández, R., & Metzger, B. D. 2013, *MNRAS*, **435**, 502
 Freiburghaus, C., Rosswog, S., & Thielemann, F.-K. 1999, *ApJL*, **525**, L121
 Goriely, S., Bauswein, A., & Janka, H.-T. 2011, *ApJL*, **738**, L32
 Goriely, S., Bauswein, A., Janka, H.-T., et al. 2014, in AIP Conf. Ser. 1594, ed. S. Jeong et al. (Melville, NY: AIP), 357
 Goriely, S., Bauswein, A., Just, O., Plumbi, E., & Janka, H.-T. 2015, *MNRAS*, **452**, 3894
 Goriely, S., Chamel, N., & Pearson, J. M. 2010, *PhRvC*, **82**, 035804
 Gould, R. J. 1975, *ApJ*, **196**, 689
 Green, J., Schechter, P., Baltay, C., et al. 2012, arXiv:1208.4012
 Grossman, D., Korobkin, O., Rosswog, S., & Piran, T. 2014, *MNRAS*, **439**, 757
 Harry, I. W., & Fairhurst, S. 2011, *PhRvD*, **83**, 084002
 Heitler, W. 1954, Quantum Theory of Radiation (3rd ed.; Oxford: Clarendon)
 Holz, D. E., & Hughes, S. A. 2005, *ApJ*, **629**, 15
 Hotokezaka, K., Kiuchi, K., Kyutoku, K., et al. 2013, *PhRvD*, **87**, 024001
 Hotokezaka, K., Wanajo, S., Tanaka, M., et al. 2016, *MNRAS*, **459**, 35
 Huba, J. D. 2013, NRL Plasma Formulary (Palm Springs, CA: Wexford College Press)
 Jackson, J. D. 1999, Classical electrodynamics (3rd edn.; New York: Wiley)
 Just, O., Bauswein, A., Ardevol Pulpillo, R., Goriely, S., & Janka, H.-T. 2015, arXiv:1504.05448
 Kasen, D., Badnell, N. R., & Barnes, J. 2013, *ApJ*, **774**, 25
 Kasen, D., Fernández, R., & Metzger, B. D. 2015, *MNRAS*, **450**, 1777
 Kasen, D., Thomas, R. C., & Nugent, P. 2006, *ApJ*, **651**, 366
 Kasliwal, M. M., & Nissanke, S. 2014, *ApJL*, **789**, L5
 Kiuchi, K., Cerdá-Durán, P., Kyutoku, K., Sekiguchi, Y., & Shibata, M. 2015, *PhRvD*, **92**, 124034
 Kiuchi, K., Kyutoku, K., Sekiguchi, Y., Shibata, M., & Wada, T. 2014, *PhRvD*, **90**, 041502
 Kochanek, C. S., & Piran, T. 1993, *ApJL*, **417**, L17
 Korobkin, O., Rosswog, S., Arcones, A., & Winteler, C. 2012, *MNRAS*, **426**, 1940
 Kyutoku, K., Ioka, K., Okawa, H., Shibata, M., & Taniguchi, K. 2015, *PhRvD*, **92**, 044028
 Lattimer, J. M., & Schramm, D. N. 1974, *ApJL*, **192**, L145
 Lattimer, J. M., & Schramm, D. N. 1976, *ApJ*, **210**, 549
 Li, L.-X., & Paczyński, B. 1998, *ApJL*, **507**, L59
 Liu, M., Wang, N., Deng, Y., & Wu, X. 2011, *PhRvC*, **84**, 014333
 Lucy, L. B. 2005, *A&A*, **429**, 19
 Mendoza-Temis, J. d. J., Wu, M.-R., Langanke, K., et al. 2015, *PhRvC*, **92**, 055805
 Metzger, B. D., Bauswein, A., Goriely, S., & Kasen, D. 2015, *MNRAS*, **446**, 1115
 Metzger, B. D., & Berger, E. 2012, *ApJ*, **746**, 48
 Metzger, B. D., Martínez-Pinedo, G., Darbha, S., et al. 2010, *MNRAS*, **406**, 2650
 Milne, P. A., The, L.-S., & Leising, M. D. 1999, *ApJS*, **124**, 503
 Möller, P., Nix, J. R., Myers, W. D., & Swiatecki, W. J. 1995, *ADNDT*, **59**, 185
 Nakar, E., & Piran, T. 2011, *Natur*, **478**, 82
 Narayan, R., Paczynski, B., & Piran, T. 1992, *ApJL*, **395**, L83
 Nissanke, S., Kasliwal, M., & Georgieva, A. 2013, *ApJ*, **767**, 124
 Paczynski, B. 1986, *ApJ*, **308**, L43
 Perego, A., Rosswog, S., Cabezon, R. M., et al. 2014, *MNRAS*, **443**, 3134
 Piran, T., Korobkin, O., & Rosswog, S. 2014, arXiv:1401.2166
 Pritychenko, B., Běták, E., Kellett, M. A., Singh, B., & Totans, J. 2011, *NIMP*, **640**, 213
 Roberts, L. F., Kasen, D., Lee, W. H., & Ramirez-Ruiz, E. 2011, *ApJL*, **736**, L21
 Rosswog, S., Liebendorfer, M., Thielemann, F.-K., et al. 1999, *A&A*, **341**, 499
 Schenter, G. K., & Vogel, P. 1983, *NSE*, **83**, 393
 Schiavietz, G., & Grande, P. L. 2001, *NIMPB*, **175**, 125
 Segré, E. 1977, Nuclei and Particles (2nd edn.; New York: Benjamin-Cummings)
 Sekiguchi, Y., Kiuchi, K., Kyutoku, K., & Shibata, M. 2015, *PhRvD*, **91**, 064059
 Sekiguchi, Y., Kiuchi, K., Kyutoku, K., Shibata, M., & Taniguchi, K. 2016, arXiv:1603.01918
 Seltzer, S. M., & Berger, M. J. 1986, *ADNDT*, **35**, 345
 Soares-Santos, M., Kessler, R., Berger, E., et al. 2016, arXiv:1602.04198
 Tanaka, M., & Hotokezaka, K. 2013, *ApJ*, **775**, 113
 Tanvir, N. R., Levan, A. J., Fruchter, A. S., et al. 2013, *Natur*, **500**, 547
 Wanajo, S., Sekiguchi, Y., Nishimura, N., et al. 2014, *ApJL*, **789**, L39
 Wang, M., Audi, G., Wapstra, A., et al. 2012, *ChPhC*, **36**, 1603
 Ziegler, J. F. 1980, The Stopping and Ranges of Ions in Matter, Vol. 5 (Oxford: Pergamon)